Study of creep cavitation behavior in tempered martensitic steel using synchrotron micro-tomography and serial sectioning techniques

Gupta, C.
Department of Mechanical Engineering, Toyohashi University of Technology

Toda, Hiroyuki
Department of Mechanical Engineering, Toyohashi University of Technology

Schlacher, C.
Institute for Materials Science and Welding, Graz University of Technology

Adachi, Y.
Department of Mechanical Engineering, Kagoshima University

他

https://hdl.handle.net/2324/1812228

Study of Creep Cavitation behavior in Tempered Martensitic Steel using Synchrotron Microtomography and Serial Sectioning Techniques

C. Gupta[1], H. Toda[1], C. Schlacher[2], Y. Adachi[3], P. Mayr[4], C. Sommitsch[2], K. Uesugi[5], Y. Suzuki[5], A. Takeuchi[5], M. Kobayashi[1].

[1]*Department of Mechanical Engineering, Toyohashi University of Technology, Toyohashi 441-8150, Japan.*

[2]*Institute for Material Science and Welding, Graz University of Technology, Kopernikusgasse, 24/l A- 8010 Graz, Austria.*

[3]*Department of Mechanical Engineering, Kagoshima University Korimoto 1-21-24,Kagoshima, 890-8580, Japan.*

[4]*Department of Manufacturing and Welding Engineering, Chemnitz University of Technology, Reichenhainer Straße 70, 09126 Chemnitz, Germany.*

[5]*Japan Synchrotron Radiation Research Institute, Sayo-gun, Hyogo 679-5198, Japan.*

[#]*corresponding author email: joy_gupta71@yahoo.co.in*

Keywords : Creep Cavitation; X-ray microtomography; Serial Sectioning; Tempered Martensitic steel

Abstract

Two three – dimensional (3-D) techniques, namely X-ray microtomography and serial sectioning, have been applied for characterization of creep cavitation behavior in tempered martensitic steel. For this purpose samples have been extracted from a series of specimens that were subjected to creep tests over the stress range 120-180 MPa at 600°C. The presence of creep voids in the series of samples was un-ambiguously detected in a non-destructive manner using synchrotron X-ray microtomography with a resolution of 1μm. The 3-D visualization of the datasets provided a quantitative assessment of the spatial distribution and morphology of the creep voids as a function of creep stress and high temperature exposure time. The quantitative analyses of the image datasets enabled the development functional relationships between the macroscopic creep test results such as rupture ductility, applied stress, creep life and cavitation characteristics such as volume fraction, and number density. The quantitative analysis also provided an assessment of manifestations of growth and coalescence processes in the respective datasets. A transition of cavitation behavior of the steel has been found to occur in the stress range 120 – 150 MPa. The evolution in the pattern of cavitation and its relation to the prior-austenite boundary was explored by combining micro-tomography and serial sectioning techniques, which revealed a new possibility in the progress of cavitation in long term creep exposed specimens of 9-12%Cr heat resistant steels.

1 Introduction

Tempered martensitic steels for advanced fossil power plant applications derive creep resistance predominantly from fine scale microstructure (martensitic laths with sub-grain structure) and from the presence of precipitates located at various internal interfaces (prior austenite, packet & lath and sub-grain boundaries) [1-3]. During high temperature exposure coarsening of the substructure network occurs towards the stress dependent equilibrium sub-grain values. Concomitantly, the evolution of metastable precipitates in terms of size and composition along with the appearance of intermetallic precipitates such as Laves and complex nitride Z phase takes place [3-6]. These microstructural changes have a decisive influence on degrading the creep resistance of the steel and accelerates the onset of cavitation damage and failure. Thus, in heat resistant steels creep plasticity and fractures are intimately connected to the evolution of microstructure during high temperature exposure. The various microstructural changes outlined above govern the onset of cavitation behavior [7]. The progress of creep damage in advanced tempered martensitic steels is reflected by the variation of creep rate with time or strain. In strain rate – strain format, the creep rate first reaches minimum within a short strain interval [8]. With continued exposure to stress, the creep rate increases due to the microstructure coarsening processes mentioned above and finally at large scale cavitation an asymptotic increase in strain rate occurs, which leads to fracture [7, 8]. The research into the evolution of microstructure during creep and its implications for cavitation behaviour in heat resistant steels is vital in order to have a fundamental understanding of the mechanisms of creep failures. These would ultimately lead to strategies to prolong the creep life of tempered martensitic steels for ultra-supercritical power plants.

Thus much of the research aimed at extending the temperature regime of application of tempered martensitic steels for high temperature components of advanced thermal power plants has been focused on retaining the stability of the microstructure with improved potential to provide precipitate stabilized subgrain hardening in the range 550°C – 650°C. Consequently advanced 9-12% Cr tempered martensitic steels alloyed with W, Ta, Nb, N, B, Co have been the subject of extensive investigations [6-15] for elucidating the effects of prolonged high temperature exposure (with and without stress in the range 550°C – 650°C) on the delicate balance of hardening via solute, precipitation and substructure stabilization with the softening occurring due to microstructural coarsening processes. This revival of research on the elementary process that dictates creep resistance of tempered martensitic steels, however did not place a similar emphasis on the cavitation phenomenon occurring during the creep failure of its modern counterparts. With the

availability new experimental investigative tools such as SEM-OIM, TEM along with EDX and nano-hardness measurements a few recent studies based on the application of these techniques to characterise the creep damage process have been reported in literature [16-18]. While these techniques provide new information with regard to the state of the crept microstructure, their characterisation of creep damage itself is limited by the artifacts arising from the destructive sample preparation techniques and additionally by the inability to image the complex shape, connectivity and spatial distribution of voids [19,20]. These disadvantages are overcome by non-destructive imaging of internal damage in materials. The past decade has witnessed an explosive growth in the application of X-ray micro-tomography technique using large synchrotron sources (eg. SPring-8, ESRF, APS) for studying the fracture and fatigue behaviour of engineering materials [21]. The unique capability of the synchrotron micro-tomography technique to interrogate the internal damage structure in materials non-invasively, both in post-mortem mode and in an in-situ manner, has promoted the use of the technique to understand the various failure phenomena present in structural materials [21-35]. Further, the development of techniques such as 3-D strain mapping [22], K-edge subtraction [23] and local crack driving force mapping [24] from the reconstructed images obtained from the in-situ micro-tomography experiments in synchrotron radiation facilities have provided new insights on the failure of alloys, foams and composites [25-35].

With regard to creep failure of materials a number of recent studies on brass [20,36], and copper [37] using synchrotron X-ray micro-tomography have been reported in literature that aims to provide an understanding of the evolution of damage using both in-situ tests as well as through post-mortem characterisation. While such studies can directly provide a visualization of progress of creep damage, the relationship of the evolving architecture of cavitation to the underlying microstructure is completely lacking. This is because the imaging and visualization of internal interfaces such as grain boundaries by synchrotron X-ray micro-tomography based techniques (eg. 3DXRD [38] , DCT [39] or SR-holotomography [40]) has not been applied to materials exposed to creep. This is compounded by the fact that steels are highly absorbent materials to X-rays which makes imaging of fine creep voids below micrometer length scale difficult. Further, the in-situ tests carried out on brass and copper, have provided information only on short term creep damage using miniature samples, which in case of steels would display different cavitation characteristics as creep brittleness is approached during long term creep. At low stresses, where the creep brittleness is displayed, the well-known fracture mode transition in heat resistant steels from trans-crystalline to inter-crystalline nature of failure occurs which has not been characterized before using x-ray micro-tomography. Because

of these reasons the observations of creep cavitation in heat resistant steels by ex-situ micro-tomography in 3D are valuable and yield important information for furthering the understanding the underlying mechanisms of damage and promote the development of new micro-mechanical models that use the quantified cavitation characteristics determined non-destructively to predict the creep life of these classes of steels. In recent times a revival of the traditional technique of serial sectioning has occurred enabled by the availability of automated units for controlled material removal, image capture and processing to provide 3D datasets containing damage and microstructural information such as grain interfaces and orientations of materials [41,42]. Serial sectioning and micro-tomography has been earlier used in a complementary manner to study the 3D morphological characteristics of Si and Ni-aluminide phases in Al-Ni piston alloy in the as-cast and solution treated conditions [43]. While synchrotron micro tomography was used to quantify the connectivity, shape and volume fraction of the two phases, their contiguity was assessed by serial sectioning. In the present paper the two techniques are combined for the first time to study the cavitation behavior of a tempered martensitic steel, crept over range of stresses and clarify the role played by internal interfaces in a mechanistic manner.

Recently, it has been possible to use X-ray micro-tomography at large synchrotron sources for characterising ex-situ creep damage *in steels* at micro-meter resolution length scale [44-46]. An example of this is a recent investigation on the development of creep damage (voids and cracks) in a Fe-Ni-Cr fully austenitic steel using synchrotron beam line at Spring-8, which provided quantitative characterization of the void content in the as-cast and ex-service variants of the material [46]. Creep voids in tempered martensitic steel have been characterized at ESRF beam line ID19 [45] on tomographic sample extracted from notched tensile specimen. In this paper, the high resolution (~1μm) synchrotron micro-tomography (SR-μCT) available at beamline BL20XU, SPring-8, has been used to characterize pattern of cavitation in crept samples of advanced 9-12%Cr tempered martensitic steel in an ex-situ manner. The aim of the investigations was to determine the nature of the spatial distribution and 3D cavitation characteristics of the creep voids with increasing creep exposure times and provide an understanding of their association with the underlying microstructure. For this purpose a series of samples extracted from crept specimens with different high temperature exposure time was characterized using synchrotron X-ray micro-tomography. Subsequently one of the samples was subjected to serial sectioning technique to generate 3D volume dataset of the grain boundary. The combined application of the two techniques provided and understanding on the way in which cavities are patterned along internal

interfaces during long term creep. Quantitative functional relations are also developed between macroscopic creep properties and internal cavitation characteristics as a function of creep exposure time.

2. Experimental Methods

2.1 Materials

The tempered martensitic steel selected for the investigation is denoted as CB8, developed in the COST program, which is a (Mo + Co) alloy variant of 9-12%Cr steel with 610 ppm Nb, 100 ppm B, 240ppm N and 260 ppm Al. The detailed chemical composition is given in table 1 [47]. The compositional modification of the steel are aimed to display enhanced high temperature microstructure stability by the presence of fine Nb and B based precipitates $(M_{23}(C,B)_6)$ and through influencing the kinetics of both laves phase $(Fe_2Mo)$and carbide coarsening by additions of Co and B respectively. The steel has been exposed to creep deformation after quenching and tempering treatment involving austenitising at 1100°C for 8 hours, followed by tempering at 730°C for 36 hours.

2.2 Creep Tests

The creep tests were carried out with periodic interruptions to measure creep strain, until failure at 600°C during loading at nominal initial stress range of 120 – 180 MPa. The diameter on companion specimens was varied in the range 7.64-9.65 mm, to define the prescribed level of stress to be imposed under a constant on-axis load of 8.25kN. The nominal diameter to gauge length ratio was kept at five. The creep tests were performed according to DIN EN10921-01.

2.2 Synchrotron Microtomography (SR-μCT)

In order to investigate the internal damage due to creep using SR-μCT, sample coupons with a square cross-section of about 300x300 μm² were extracted from the crept specimen near (less than 5 mm) to the fracture surface. A schematic of the location of the sample with respect to loading direction and fracture surface is shown in figure 1. Such small sample coupons were used for the ex-situ tomography examination as the absorbtion of steels to X-rays are very high. The samples were cut in the transverse direction to the loading axis at close proximity to the fracture surface in order to maximize the sampling of representative cavities that participated in the creep fracture. Although, this method could facilitate the sampling of cavities near to the locations where reductions of diameter

after fracture were measured due to the small size of the sample accurate correlation between the two was not possible. Further, the irregular nature of the fracture plane precluded preparation of uniform thickness of transverse samples containing the fracture surface, which could prevent high quality tomography images to be obtained. This would hinder the visualization of fine creep voids in dense material such as steel illuminated by a monochromatic synchrotron beam. Hence very fine slices close to the fracture surface was used for tomographic scans.

The SR-µCT on the extracted samples was performed at the undulator beam-line BL20XU of the SPring-8. A monochromatic X-ray beam produced by a liquid nitrogen-cooled Si (511) - (333) double crystal monochromator, was tuned to produce a beam of energy 40 keV. An image detector system, placed 110 mm from the sample, consisted of a cooled 4000 (H) × 2624 (V) element CCD camera (effective pixel size of the camera: 5.9 µm, used in 2 x 2 binning mode), a LSO:Ce scintillator (Lu_2SiO_5:Ce) and a relay lens (×20). In total, 1500 radiographs, scanning 180 degrees, were obtained in 0.12-degree increments. The exposure time for a single shot was kept at 300 ms. The large distance between the sample and detector enabled the projection data to capture both absorption and phase information that enhanced the detectability of the cavitation voids [25]. Theoretical limit of this projection-type SR-µCT set-up is approximately 1 µm, which is determined primarily by inevitable image blurring caused by the Fresnel diffraction, the diffraction limit of visible light and the spatial resolution of a scintillator [48]. Isotropic voxels (a volume element in 3D space) with 0.5 µm edges were achieved in the reconstructed slices that were at least necessary to achieve the 1 µm spatial resolution [44]. A convolution back projection algorithm was used for achieving the reconstruction and the analysis of the reconstructed slices for various damage characteristics were executed in customized software.

In order to extract the creep cavities for analysis, a local threshold of grey value was assigned and only those greater than 3^3 connected voxels were selected. Investigations by Phillion et. al. [49] and Landron et. al [50] showed the influence of resolution using tomography setups that gave different voxel sizes, on the quantitative analysis of the 3D datasets. This problem is minimal in this case, as all the experiments were carried out in the same identical set up. Hence applying the procedure resulted in cavities smaller than 27 (1.5 x 1.5 x 1.5 µm) connected voxels to be ignored for the analysis so that a conservative quantitative estimate of the cavitation parameters could be derived. It is to be mentioned here that this minimum threshold voxel limit of void size used for quantitative analysis is more than twice that used by Sket et. al. [45] for ex-situ investigations on creep deformed E911 steel (which was 8 voxel or 0.66 µm). The analysis

software implemented the marching cubes algorithm to determine the number, volume, surface area and co-ordinates of the center of mass of each void present in the reconstructed region of interest.

2.3 Serial Sectioning

In order to carry out the serial sectioning one of the samples that was subjected to tomographic scan was mounted using a conducting resin powder after fixing in a steel spring. This was done to ensure no lateral movement of the sample during serial sectioning procedure. The serial sectioning steps involved placing micro-hardness indents on the sample, followed by manual polishing for appropriate time, and then measuring the decrease in indent sizes to determine the amount of thickness polished out. At desired intervals optical microscopy was done both before (as polished) and after etching stages. The etching was carried out using a special solution comprising of 100 ml ethanol, 10g picric acid and 2 ml HCl, which was found to reveal prior-austenite grain boundaries in the steel under investigation [51]. In this manner a series of slices was obtained with a constant pitch that interrogated the required volume of the sample. In this case the pitch size was 3µm and the serial sectioning was carried out for about 60µm depth on the sample which was crept for 15216 hours. The etch slices were used to manually delineate the austenite boundary which were then transferred to the as polished slice section. The as polished slices were then merged to create a volume dataset of the austenite boundary. In order to locate the austenite boundary in the tomography dataset, one polished section of the selected sample about 9 µm from the top containing the boundary was overlaid on the tomography dataset on the basis of matching locations of the voids seen in the respective slices.

3. Results

3.1 Creep Test

The creep test results are summarized in figure 3 in the form of variation of minimum creep rate ($\dot{\varepsilon}_{min}$), Larson-Miller (LM) parameter and rupture ductility with initial stress. A linear relationship is clearly evident between $\dot{\varepsilon}_{min}$ and Larson-Miller (LM) parameter

(Constant = 20), and the applied stress. Further, it can be seen that the rupture ductility decreases as the applied stress is reduced from 180 MPa to 120 MPa. The stress exponent has been calculated from the $\dot{\varepsilon}_{min}$ - σ plot as 17.8. This value is in the range typical for precipitation hardened materials in the high stress regime where the tertiary creep governs creep life [52]. In tempered martensitic steels the tertiary regime can be distinguished into two regions – a coarsening dominated region and a cavitation dominated region [8]. The sharp rise in the tertiary creep rates in the cavitation dominated regime distinguishes the former from the later. It is to be noted that two regions do not represent exclusivity in the operation of the microstructure coarsening and cavitation phenomena. In the coarsening dominated regime cavitation could occur but its effect on the creep would be minimal. The cavitation dominated region would be distinguished by the steep rise in creep rate to greater levels than those in the coarsening stage. As enhanced creep rates would mean rapid elongation over short time, it is reasonable to propose that a simple tangent intersection in the elongation-time plot obtained from creep test (as shown in the inset of figure 3) can estimate the point where the cavitation dominated region commences. The purpose of such an exercise is to assess the fraction of the creep life expended in damage led increase in creep rate before fracture. The plot of the ratio of the of the cavitation dominated region in tertiary stage to the creep life as a function of applied stress is shown in figure 3 as plot of variation T_D/T_F ratio with applied stress. The numerator (T_D) of the ratio represents the time taken from the tangent intersection point to fracture and the denominator (T_F) represents the total creep life. It is clearly seen that there is a sharp decline in the ratio as creep stress reduces from 180 to 120 MPa. This conclusively shows that the as the creep exposure time increases at lower stress there is decrease in the fraction of the creep life devoted for cavitation damage before fracture. It is of significance to point out that the fracture surface observations after creep in the stress ranges 120-180 MPa at 600°C for CB8 steel was found to be increasingly inter-granular below 165 MPa. The presence of inter-granular fracture is an indication of creep brittleness and could be responsible for the decrease in the T_D/T_F ratio with stress.

3.2 Micro-tomography – 3D Visualisation

A typical reconstructed slice containing creep voids in the 8 bit grey scale format is shown in figure 4. The slice shows the square sample cross-section of steel matrix containing creep voids that appear as black spots of different shapes. The influence of deflection contrast is also seen as a bright halo surrounding these black spots. This is shown in figure 4 (b) by the arrows pointing to 'A'. The precipitous drop in the electron densities at the interface between creep voids and steel matrix, results in a significant

phase modulation of the incident coherent X-ray beam, as it passes through the sample. As a result a strong deflection contrast at creep void borders develops, which when superimposed on the conventional absorption contrast produces a strong signature of the edges [19]. In the present case the grey scale is mapped in an inverse manner to the intensity distribution captured at the detector, as a result of which the superimposed absorption and deflection contrast at the void edges appears as higher grey level values than the matrix in the reconstructed slices. The 3D rendering of the reconstructed slices obtained from SR-μCT scans on the samples tested over stress range 120 – 180 MPa is shown in figure 5. It can be clearly seen that the creep damage that is heterogeneously distributed in the reconstructed volume of interest is progressively increasing with longer creep exposure times. Appearance of regions containing void clusters increases especially for the sample that has been exposed to maximum creep time. At creep exposure times over the stress range 150 - 180 MPa the creep voids seem to be quite sparsely distributed within the reconstructed volume. The creep voids in all the datasets are seen to be aligned as a chain of voids, despite the widespread cavitation within scanned volume at the lower stresses. At lower stresses the presence of large complex shaped voids as well as multi-lobed voids can be clearly seen. Figure 6 shows a few close up renderings of these complex voids visualized in the sample exposed to creep for the longest time. These range from being multi-lobed chain of voids to a complex void cluster near a large oblate shaped void. The observation of multi-lobed morphology of voids suggests the operation of void coalescence processes in their formation.

3.3 Micro-tomography – Quantitative Analysis

The quantitative analysis results are shown in figure 7, in terms of variation of number density, size and volume fraction of voids with the applied creep stress and creep exposure time. These characteristics have been computed from the individual void features quantified in terms of volume, surface area and size for each of the datasets obtained from SR-μCT. While a steady rise in the number density of voids is seen with decreasing creep stress, correspondingly a significant rise in the void volume fraction is observed only for the lowest stress, which had the maximum creep life.

At the lowest stress there has been nearly three-fold increase in volume fraction along with slight increase in the average diameter of voids and a significant upswing in the number density curve. In case void growth and coalescence dominates over nucleation, then it is expected that the void volume fraction should increase at the expense of number density. In the present study, while both the parameters increase, the void volume fraction increases much more rapidly than number density. This could imply that the void growth

9

by coalescence is progressively strengthened over nucleation as the stress is reduced in the range 120-180 MPa. This is also corroborated by the presence of many of complex shaped large voids at the lowest stress (figure 6). It is also of significance to note that at the lowest stress the void morphology consisted of both ellipsoid as well as complex multi-lobed shapes.

The functional relationship between the intrinsic cavitation characteristics and macroscopic creep ductility over the stress range 120 – 180 MPa can now be quantified. The plot between void volume fraction and number density with rupture ductility has been shown in figure 8. It can be clearly seen that these cavitation characteristics undergo a transition as the creep ductility is reduced in the stress range 150 – 180 MPa. At rupture ductility ranges above 14% which was obtained in the stress range 150 – 180 MPa, both void volume fraction and number density are found to be at low levels. At lower stress ranges where a significant drop in the rupture ductility has been found, these cavitation parameters dramatically increase in an exponential manner. The exponential fit correlating the dependence of rupture ductility on the cavitation parameters (void volume fraction, ν and number density, η) are given below :

$$\nu = 165.76 + 6.7\text{x}10^8 \exp(-1.91\Lambda) \qquad (1)$$

$$\eta = 0.399 + 7.0 \exp(-0.33\Lambda) \qquad (2)$$

Where ν = void volume fraction in ppm; η = number density in $10^{-5}\mu\text{m}^{-3}$; Λ = rupture ductility in %. These parameters provided a quality of fit (R^2) value of 0.94 It is also to be noted from the exponential powers that the rupture ductility is more sensitive to increases in void volume fraction as compared with void number density.

The analysis of the void size distribution is shown in figure 9. It is clearly seen that as the creep stress reduces the peak frequency of void size both increases in magnitude and also shifts towards larger void size values. This result lends support to the suggestion that the intense cavitation at low creep stresses is due to nucleation of new voids along with increasing influence of void coalescence. This interpretation stems from the observation that samples subjected to creep stress in the range 120 – 180 MPa shows no such shifts in size distribution until 120 MPa with increasing peak frequencies. It needs to be mentioned here that the distribution obtained for specimen crept at 165 MPa is fortuitous

and is probably an effect of extracting the sample for ex-situ tomography imaging. Despite this, the general trends in the variation of cavitation characteristics can be discerned in this study using a series of creep exposed samples.

The quantitative assessment of heterogeneity of spatial distribution in 3D datasets has been made in earlier studies [53]. These studies have been applied on densely populated datasets with spherical particles. Parameters from image analysis techniques such as co-variance, two point correlation function, pair correlation function etc essentially provides different estimations of a probability of proximity of objects in 3D datasets. In case of sparsely populated datasets containing irregular shaped objects the applicability of these parameters needs to be established. Further the computation complexity of estimating these parameters are quite significant. The heterogeneity in spatial distribution arises due to an anisotropic occurrence of objects in one or more directions. Anisotropic occurrence of objects in more than one direction leads to clustering. From the observation of the 3D visualization of datasets it appears that clustering of voids seems more likely to occur as the creep stress reduces. Thus by converting the void co-ordinates to their position vector representation, the heterogeneity would be manifested as a cluster of position vector points. These statistics can be easily captured by dividing the position vector space equally into regions of prescribed size and counting the void number in each region. Figure 10 (a-c) shows the variation in the fraction of voids sampled locally when the position vector space is divided into 20 contiguous regions for three datasets. The positions of clustering are evident by the peaks displayed in the plots above the fraction computed if the voids were uniformly distributed. From these plots a clustering index can be derived for each dataset characterized at the respective stress using the following formulas

$$\text{CI} = \text{var } \{f_n^i - \bar{f}_n\} \qquad (1)$$

$$\bar{f}_n = \frac{1}{n} \qquad (2)$$

$$f_n^i = \frac{n_i}{N} \qquad (3)$$

Where CI = clustering index

$\{f_n^i\}$ = fraction of voids occurring within the ith region.

var $\left\{f_n^i - \bar{f}_n\right\}$ = variance of the set of difference between the fraction of voids in a ith region to the average fraction computed using (3)

n = number of regions ; N = total number of voids in the dataset.

Figure 11 (a) shows the variation of the clustering index with applied stress. It is seen that the clustering index of 3D datasets increases as the stress reduces, thereby quantifying the degree of heterogeneity with decrease of stress in the range 120-180 MPa. The assessment of the void sizes in each of the local regions has been also carried out, from which the fraction of the voids above the dataset average void size was computed. The variation of the fraction of voids above average size occurring in the cluster regions of respective datasets is also shown in figure 11(a). It is seen that with decrease in stress, the fraction of voids in the clusters that are above the respective dataset average increase. As both the parameters increase with decrease of applied stress, a strong correlation between them is implied. Accordingly a scatter curve between the above two parameters is shown in the figure 11(b), which clearly shows strong quantifiable correlation. Hence it can be concluded that the presence of voids greater than the dataset average in the clusters cause increase in the heterogeneity of spatial distribution.

The measurements of the total void volume, average volume and sphericity (computed as ratio of surface area to volume of void) as a function of the void size range can provide important insights on the mechanisms of nucleation and growth during creep. Landron et. al. [54, 55] studied the ductile fracture of dual phase steel at room temperature using in-situ synchrotron micro-tomography. The evolution of void number density, shape and size were used to characterize and model the nucleation and growth behavior of DP steel during ductile fracture. While in-situ test provides a time scaled dataset series by a single test, ex-situ tomography scans of a series of samples crept over a range of stresses can provide similar information as the datasets would be related in terms of a systematic variation of failure life, commonly represented by the Larson-Miller parameter plot with applied stress. In this case the time scale varies from 2825 hours (or ~120 days) to 51406 hours (or ~ 6 years). It is to be emphasized that it is practical that datasets related at this wide range of time scale be obtained by ex-situ scans and not from in-situ tests. Creep failure by cavitation is also caused by nucleation, growth and coalescence of voids. Due to the operation of these processes the increase in void size occurs with characteristic effects on its volume fraction and sphericity. For example a dataset which has dominant nucleation effects would result in greater increase in number density than the volume

fraction. Void size increases by growth, coalescence or both would be accompanied with reduction in number density, increase in volume fraction and changes in the void shape from acicular to oblate spheroids (i.e. increase in sphericity value). The determination of the overall variation of void size distribution and number density is inadequate to bring out the extent to which these processes are manifested in a given dataset. Rather, mapping the variation of void volume fraction and sphericity across the void size distribution can reveal whether void nucleation or growth and coalescence processes dominate. Figure 12 shows the plots of total void volume and average void volume as a function void size for each of the datasets quantitatively analyzed of samples crept to failure at stress range 120 – 180 MPa. It is seen that in all cases the average void volume increases with increasing void size range with intermittent peaks (figure 12). However the total void volume for each dataset as a function of size range first increases until it reaches near to its respective peak frequency size range (figure 9). Subsequently, at larger void sizes the total void volume first sharply drops, and then either continues to display a gradual downward trend or an upward trend depending on the stress level during the creep testing. While a gradual upward trend is seen for the creep stress levels of 180 MPa and 165 MPa, a lower trend is observed for the cases crept at lower stress levels. In all cases intermittent peaks are prominently seen in the void size ranges beyond the respective peak frequency size. These peaks suggest that both growth of individual voids and coalescence existing voids occurs for the associated void size ranges. The measurements of sphericity as a function of void size is shown in figure 13. It can be seen that for all the datasets below its respective peak size range there increase in sphericity of voids. Above the peak size however, the sphericity characteristic undergoes alternating increasing and decreasing trend for all datasets. As sphericity values represent the morphological shape of object, this variation suggests that a transition in void shape occurs as they increase in size, from being acicular to spheroidal and back to acicular. The cyclical transition in shape with increase in size could be the result of sampling of voids that grow under the action of grain boundary sliding. This hypothesis would be strengthened if the void size correlates negatively with sphericity parameter in the datasets. The figure 13 (b, c) shows the variation of correlation coefficient plotted along with the average sphericity and fraction of voids sampled in each size range. It is clearly seen that the correlation coefficient above the peak void size range transitions to negative values. The negative correlation of sphericity with void size implies that as growth occurs the void shape tend towards being acicular rather than being spheroidal. This can be rationalized as the growth of creep voids under the influence of grain boundary sliding. As the size grows inevitably the adjacent voids impinge and coalesce resulting in the change in the void shape towards spheroidal shapes and increase

in sphericity. Thus the cyclical variation in sphericity could be due to the combined action of void growth and coalescence.

These trends suggest that at the void size range below the peak frequency size range there could be predominately rapid growth of the voids as both total void volume and average void volume increase. The larger void sizes than the peak frequency size could be formed mostly by a combination of growth and coalescence of voids due to the observed divergent trends in the above two parameters and the cyclical variation of sphericity parameter. A threshold void size can be defined beyond which the void sizes are undergoing growth and coalescence rather than nucleation and growth. The point of transition of the sphericity parameter from positive to negative values can serve as the criteria for threshold size beyond which coalescence operates. Thus a coalescence affected fraction has been determined and plotted as a function of applied stress in figure 14. It is evident that there is clear increase in the coalescence fraction as the stress is lowered in the range 165-120 MPa. It is to be noted that these results restricts the computation of void growth rate for void size range upto only about 4 μm (depending the respective creep stress), where nucleation and growth operate. This is consistent with the studies of Wu and Sandström [52] where the growth rate of creep voids upto 2.5 μm in Cr-Mo-V steel at 600°C were reported. The trends observed in the quantitative characteristics of cavitation with stress, exposure time and void size as well as the morphology of the creep voids at 120 MPa, suggests that the increase in cavitation at the lowest stress occurs due to both nucleation of new voids as well as growth and coalescence of the voids formed perhaps at the early stages of the creep life of the steel.

3.4 Micro-tomography and Serial Sectioning

In order to associate the void formation with the underlying microstructure serial sectioning was carried out on the sample crept at 150 MPa to failure in 15316 hours. The result from the serial sectioning technique is shown in figure 15 where it is seen that the prior austenite boundary is completely reconstructed. It is clearly seen that the shape of the prior austenite boundary is quite complex and tortuous. In order to relate the volumes seen in the micro-tomography with that of the serial sectioning, the voids visible in the respective datasets were matched. The matching regions are shown in the composite image, figure 16 comprising of the micro-tomography and serial sectioning dataset. From the figure it appears that void cluster marked as 'A' is associated with the prior austenite grain boundary. As it is the dominant cluster type in the volume, it may well be that in this case that voids show preference to nucleate at the prior austenite boundary as

compared with packet or lath boundary located in the grain interior.

The rendered 3-D volume expanded near to regions of high density of cavitation for the samples exposed to creep times of 15316 hour and 51406 hours are shown in figure 17. The contrast in the spatial alignment of the chain of voids of the two cases is clearly evident, which have been emphasized by the black lines in the images. These lines represent the voids aligned inside the reconstructed region seen visually after 3D rendering. In the dataset obtained from the sample crept only upto 15316 hours show alignments in narrow regions of the dataset, which has been found from the serial sectioning technique to lie along the prior austenite boundaries. In the other case the cavitation is far more proliferated. It needs to be mentioned that the specimen dimensions were smaller than the prior austenite grain size of 600μm in the crept structure. However, the objective was of the study was characterize the nature of cavitation with stress and creep exposure time. As all the samples contained prior austenite boundaries and grain interior interfaces it was possible to characterize the overall cavitation behavior in the steel. From the fact that the austenite grain size is about 600μm in the crept microstructure, the aligned voids for the sample crept for 51316 hours at 120 MPa, could be interpreted as being within the grain interior interfaces such as packet or lath boundaries. This is because the spacings between the rows of aligned voids clearly are much less than the prior austenite grain size. Moreover the etched optical micrographs of two regions of the sample crept at 120 MPa, shown in figure 18 clearly reveals the presence of large number of cavities in the grain interior. The prior austenite boundaries are highlighted in these images from which it is clear that the nature of void alignment shown in the dataset in fig 17 (b) does not follow the prior austenite boundary shape. These results suggest that as creep brittleness is approached in CB8 steel over stress range 120 – 180 MPa, the grain interior interfaces show significant cavitation.

4. Discussion

The investigation of creep behaviour in CB8 steel by combining micro-tomography and serial sectioning techniques on a series of samples extracted from specimens crept in the stress range 120-180 MPa, facilitated the elucidation of damage mechanisms in terms of 3D cavitation characteristics. The basic creep behavior of CB8 steel at 600°C in the stress range of 120 MPa – 180 MPa was found to be a steady decrease in LM parameter, sharp reduction of rupture ductility and the fraction of creep life spent in the cavitation dominated regime. The 3D datasets obtained from the tomography scans on transversely

oriented samples enabled visualization of in-homogenous spatial distribution of creep voids as a function of stress. The increasing intensity of cavitation was clearly visible in the dataset series and correlated with the decrease in rupture ductility. The correlation of decrease in rupture ductility with increase in cavitation is consistent with earlier investigations on low alloy steels and 9-12% Cr martensitic steels [52,56-57]. The distinguishing feature of creep cavitation revealed by 3D visualization of the datasets, was the fact that they predominantly occurred as a chain of voids in contrast to damage developed during tensile fracture at room temperature in CrMoV steel [58], where such alignment is not strongly evident.

Quantitative analysis of the datasets not only characterized the overall cavitation behavior in terms of void volume fraction, size distribution and number density, but also provided information on local cavitation characteristics that enabled a mechanistic interpretation of data. A transition of cavitation behavior was clearly displayed by an exponential rise in the void volume fraction and number density with decrease in stress. Local visualization of voids clusters seen in the dataset obtained from the sample crept at 120 MPa showed the presence of numerous multi-lobed void structures. The heterogeneity of cavity spatial distribution seen in the respective datasets was quantitatively characterized using a clustering index parameter. The clustering index correlated strongly with the increasing presence of cavities above the peak void size frequency range within the ensemble of void clusters. Considering these observations, it can be concluded that the formation of ensemble of void clusters at lower stress led to the increase in not only heterogeneity of cavity distribution but also a dramatic rise in void volume fraction and increase in void size. The overall quantitative analysis of the datasets also revealed that there is a significant rise of the void number density. It is quite well known that creep void nucleation is governed by thermodynamic considerations in the nanometer range [52, 56, 59]. However, the observable creep voids using optical microscopy have been shown to commence in the tertiary regime of CrMoV steels from strains close to the attainment of minimum creep rate by Eggeler et. al. [56]. The presence of nano-meter size cavities in the present case may have little significance on the creep properties of the steel, as seen by the linear $\dot{\varepsilon}_{min}$ - σ plot. However, considering the steady rise in the void number density as the stress decreases, continuous nucleation of creep cavities from early stages of tertiary regime of creep seems a likely possibility. The results from the variation of void volume fraction and sphericity over the void size range point to the fact that the coalescence processes become stronger as the stress decreases in the range 120 – 180 MPa. The increase in the fraction of creep voids affected by coalescence attests to this

fact. Considering these trends the void number density should have reduced. The reasons for sustained rise in void number density in series of datasets displaying stronger cavity coalescence are revealed by the application of serial sectioning. The serial sectioning technique applied to the dataset obtained from creep test at 150 MPa showed that the cavitation present at narrow regions is along the prior austenite boundaries. Comparing the spatial distribution characteristics at 150 MPa to those obtained from creep specimens at 120 MPa, show that cavitation is significantly proliferated at the lower stress. The specimen size for tomography scans were considerably less than the average prior austenite grain diameter measured after creep, which meant that the samples in the datasets contained only small regions of austenite boundaries and a large number of grain interior interfaces (packet and lath boundaries). The change in presence of creep cavities from narrow regions (as in 150 MPa) to wider locations across the sample inevitably implies that packet and lath boundaries have cavitated at the lower stresses. Thus although the coalescence affected fraction increased in the dataset obtained from decrease of creep stress, increase of grain interior cavitation prevented the decrease of number density. It is however to be noted that despite proliferation of cavitation in the datasets at the lower creep stress the heterogeneity of the spatial distribution of cavities in fact increased. This could be due an increase in void cluster ensembles in the datasets.

The detailed quantification of the 3D datasets followed by serial sectioning yielded several new information on the cavitation characteristics of CB8 steel which could serve as a basis to further the understanding of the well-known transition in fracture of heat resistant steels exposed to long term creep. Traditionally it has been believed that manifestation of creep brittleness to be due to nucleation and growth of inter-granular cavities, that eventually link up to form propagative cracks. The sequence of damage development have been understood as being due to cavity nucleation and growth in isolated independent micro-volumes, followed by an interaction of these micro-volumes through void coalescence and then the consequent transformation of the coalesced cavitation into a network of micro-cracks, thereby heralding the onset of final fracture [60]. In this framework the creep damage has a nucleation dominant phase and coalescence dominant phase which then transitions to onset of cracking at a set of highly cavitated austenite boundaries. This understanding is unable to predict increase of both void volume fraction, and number density, cyclical variation of sphericity and proliferation of cavitation from grain boundary to grain interior. These changes in cavitation behavior are non-trivial as it is accompanied by lower ductility and a shorter fraction of life expended in cavitation led increase in creep rate before fracture. In order to rationalize these observations obtained in the present study, a new description of the

progress of creep damage needs to be provided. The following presents a more probable sequence of progress of damage as creep brittleness is approached.

It is well known that internal interfaces of tempered martensitic steels consisting of prior austenite boundaries packet and lath boundaries are prone to cavitation. Unquestionably, the cavitating prior-austenite boundaries play a key role in the development of creep damage and failure of long term crept specimens of heat resistant steels. The breakdown of the martensitic structure, the precipitate coarsening and changing particle composition, promote the nucleation and growth of creep voids near prior-austenite boundary. As the cavitation intensifies at low stresses, the present study suggests that its nature at the prior austenite boundaries also changes and may depend on the extent of grain interior cavitation. Thus the cavitation may progress relatively slowly at the prior austenite boundary, when the grain interior is relatively unscathed; and these damage processes may be accelerated at the prior-austenite boundary when there is significant grain interior cavitation. An enhancement in cavitation at prior-austenite boundary when the grain interiors are damaged may be due to a change in the stress distribution in microstructure of the steel brought about by the reduced ability of the latter to accommodate the externally applied stress. This may lead to a synergy between the enhanced stress at the prior-austenite boundary and the grain boundary sliding to result in tortuous boundary shapes and rapid cavitation by formation of void cluster ensembles, and finally linking of these clusters leads to fracture. Thus the critical point in this sequence is the change in pattern of cavitation towards the grain interiors that accelerates the creep damage towards failure.

5. Conclusions

The various conclusions derived from the study of the creep cavitation behavior of CB8 steel as a result of high temperature exposure at 600°C, over the stress range 120 – 180 MPa investigated using two 3-D characterization techniques can be summarized below:

1. The nature of creep cavitation is in-homogenous within the volume characterized by synchrotron X-ray micro-tomography. As the creep stress decreases from 180 MPa to 120 MPa, a transition in the cavitation characteristics occurs distinguished by :
   (a) Change in the spatial distribution of cavitation in the 3-D visualized volume dataset.
   (b) Appearance of large coalesced creep voids having complex shape.
   (c) A dramatic increase in the void volume fraction and number density as a function

of applied stress and high temperature exposure time.

2. The quantitative analysis of the evolution of creep cavitation in CB8 steel in stress range 120 – 180 MPa provides an exponential relationship between void volume and number density with rupture ductility. The reduction of ductility in the stress range 120 – 150 MPa is found to be more sensitive to increase in void volume fraction as compared to the increase in number density.

3. The serial sectioning conclusively showed that the prior austenite boundary for the sample was of complex tortuous shape. On combining with the SR-μCT image it was concluded that the voids in the sample crept to failure in 15316 hours at 150 MPa were predominantly aligned along the prior austenite boundary.

4. The trends of cavitation behavior displayed by CB8 steel in the stress range 120 – 180 MPa and its quantitative relationships with the creep test results were rationalized to be a manifestation of progress of damage along the prior-austenite boundaries exacerbated by grain interior cavitation as creep brittleness is approached.

References

1. G. Eggeler, Acta Metall 37 (1989) 3225-3234.
2. Y. Wang, K. H. Mayer, A. Scholz, C. Berger, H. Chilikuru, K. Durst, W. Blum Mater Sci Eng A510-511 (2009) 180-184.
3. F. Abe, Sci Technol Adv Mater. (2008) Doi: 10.1088/1468-6996/9/1/013002.
4. A. Golpayengni, H. O. Andrén, H. Danielsen, J. Hald, Mater Sci Eng A489 (2008) 310-318.
5. A. Aghajani, C. H. Sommen, G. Eggler   Acta Mater 357 (2009) 5093-5106.
6. J. Hald   Int Jour Press Vess Pip 85 (2008) 30-37.
7. M. E. Kassner, T. A. Hayes, Int Jour Plast 19 (2003) 1715-1748.
8. S. Straub, M. Meier, J. Ostermann, W. Blum   VGB Kraftwerkstechnik 73 (1993) 646-653.
9. P. J. Ennis, A. Z. Lipic, O. Watcher, A. C. Filemonowicz   Acta Mater 45 (1997)

4901-4910.

10. D. Rojas, J. Garcia, O. Prat, G. Sauthoff, A. R. Kaysser-Pyzalla   Mat Sci Eng A528 (2011) 5164-5168.

11. D. Rojas, J. Garcia, O. Prat, G. Sauthoff, A. R. Kaysser-Pyzalla   Mat Sci Eng A527 (2010) 3864-3871.

12. O. Prat, J. Garcia, D. Rojas, C. Carrasco, G. Inden   Acta Mater 58 (2010) 6142-6152.

13. F. Abe, Mat Sci Eng A319-321 (2001) 770-778.

14. F. Abe F, Mat Sci Eng A387-389 (2004) 565-573.

15. R. Agamenone, W. Blum, C. Gupta, J. K. Chakravartty   Acta Mater 54 (2006) 3003-3014.

16. K. Fujiyama, K. Mori, Matsunaga T, Kimachi H, Saito T, Hino T, Ishhii R (2009) Mat Sci Eng A510-511: 195-201.

17. Q. Z. Chen, C. W. Thomas, D. M. Knowles Mat Sci Eng A374 (2004) 398-405.

18. K. Fujiyama, K. Mori, D. Kameko, H. Kimachi, T. Saito, T. Hino, R. Ishhii   Int Jour Press Vess Pip 86 (2009) 570-579.

19. L. Salvo, P. Cloeten, E. Maire, S. Zabler, J. J. Blandin, J. Y. Buffiere, W. Ludwig, E. Boller, D. Bellet, C. Jossenrond   Nucl. Instrum. Meth. Phys. Res. 200 (2003) 273-278.

20. F. Sket, A. Isaac, K. Dziekol, G. Sauthoff, A. Borbléy, A. K. Pyzalla   Scripta Mat 59 (2008) 558-561.

21. S. R. Stock Int Mater Rev 53 (2008) 129-181.

22. M. Kobayashi, H. Toda, Y. Kawai, T. Ohgaki, K. Uesugi, D.S. Wilkinson, T. Kobayashi, Y. Aoki, M. Nakazawa   Acta. Mater. 56 (2008) 2167-2181.

23. Q. Zhang, H. Toda, Y. Takami, Y. Suzuki, K. Uesugi K, M. Kobayashi   Philos. Mag A90 (2010) 1853-1865

24. H. Toda, S. Yamamoto, M. Kobayashi, K. Uesugi, H. Zhang   Acta. Mater. 56 (2008) 6027-6039.

25. J. Baruchel, J. Y. Buffiere, E. Maire, P. Merle, G. Peix (2000) X-ray Tomography in Material Science, HERMES science publications, Paris.

26. S. R. Stock, (2009) MicroComputed Tomography-Methodology and Applications CRC Press Boca Raton Florida.

27. F. Beckmann, R. Grupp, A. Haibel, M. Huppmann, M. Nothe, A. Pyzalla, W. Reimers, A. Schreyer, R. Zettler, Adv. Eng. Mater. 9 (2007) 939-950.

28. H. Toda, S. Masuda, R. Batres, M. Kobayashi, S. Aoyama, M. Onodera, R. Furusawa, K. Uesugi, A. Takeuchi, Y. Suzuki   Acta. Mater 59 (2011) 4990-4998.

29. H. Toda, E. Maire, S. Yamauchi, S. Tsuruta, T. Hiramatsu, M. Kobayashi   Acta.

Mater. 59 (2011) 1995-2008.

30. H. Toda, T. Nishimura, K. Uesugi, Y. Suzuki, M. Kobayashi Acta. Mater. 58 (2010) 2014-2025.

31. H. Toda, S. Yamamoto, M. Kobayashi, K. Uesugi, Acta. Mater. 56 (2008) 6027-6039.

32. E. Maire, O. Bouaziz, M. D. Michiel, C. Verdu, Acta. Mater. 52 (2008) 4954-4964.

33. J. Y. Buffiere, E. Maire, P. Cloetens, G. Lormand, R. Fourgeres Acta. Mater. 47 (1999) 1613-1625.

34. N. Limodin, J. Rethore, J. Y. Buffiere, Gravouil, F. Hild, S. Roux   Acta. Mater. 57 (2009) 4090-4101.

35. C. F. Martin, C. Josserond, L. Salvo, J. J. Blandin, P. Cloetens, E. Boller, Scripta Mater 42 (2000) 375-381.

36. A. Pyzalla, B. Camin, T. Buslaps, M. D. Michiel, H. Kaminski, A. Kottar, A. Pernack, W. Reimers Science 308 (2005) 92-95.

37. K. Dzieciol, A. Borbély, F. Sket, A. Isaac, M. D. Michiel, P. Cloetens, T. Buslaps, A. R. Pyzalla, 59 (2011) 671-677.

38. H. F. Poulson, Three -Dimensional X-ray Diffraction Microscopy: Mapping Polycrystals and their Dynamics, Springer, 2004.

39. W. Ludwig, S. Schmidt, E. M. Lauridsen, H. F. Poulson, J. Appl. Cryst. 41 (2008) 302-309.

40. C. Landron, E. Maire, J. Adrien, H. Suhonen, P. Cloetens, O. Bouaziz, Scripta. Mater. 66 (2012) 1077-1080.

41. A. A. Wahab, C. R. Hutchinson, M. V. Kral, Scripta. Mater. 55 (2006) 69-73.

42. A. A. Wahab, M. V. Kral, Mat. Sci. Eng. A412 (2005) 222-229.

43. Z. Asghar, G. Requena, H. P. Degischer, P. Cloetens, Acta. Mater. 57 (2009) 4125-4132.

44. H. Toda, F. Tomizato, M. Zeissman, Y. Besel, K. Uesugi, A. Takeuchi, Y. Suzuki, M. Kobayashi, B-F. Foit, ISIJ 52 (2012) 517-523.

45. F. Sket, K. Dzieciol, A. Borbély, A. R. Pyzalla, K. Maile, R. Scheck   Mater. Sci. Eng. A528 (2010) 103-111.

46. K. S. Cheong, K. J. Stevens, Y. Suzuki, K. Uesugi, A. Takeuchi   A513-514 (2009) 221-231.

47. G. Dimmler, P. Weinert, E. Koseschnik, H. Cerjak   51 (2003) 341-353.

48. A. Takeuchi, K. Uesugi, H. Takano , Y. Suzuki   Rev Sci Instru 73 (2002) 4246-4252.

49. A. B. Phillion, P. D. Lee, E. Maire, S. L. Cockcroft   Metall. Mater. Trans 39A (2008) 2459-2469.

50. C. Landron, E. Maire, J. Adrien, O. Bouaziz, M. D. Michiel, P. Cloetens, H.

Suhonen   Nucl Instrum Meth Phy Res B 284 (2012) 15-18 .

51. Peter M, PhD thesis titled Evolution of microstructure and mechanical properties of heat affected zone in B containing 9-12% Chromium Steels, Graz University of technology (2007).

52. R. Wu, R. Sanström Mater. Sci. tech. 11 (1995) 579-588.

53. A. Delarue, D. Jeulin, Image Anal. Stereol. 22 (2003) 153-161.

54. C. Landron, E. Maire, O. Bouaziz, J. Adrien, L. Lecorme, A. Bareggi, Acta. Mater. 59 (2011) 7564-7573.

55. C. Landron, O. Bouaziz, E. Maire, J. Adrien, Scripta. Mater. 63 (2010) 973-976.

56. G. Eggler, J. C. Earthman, N. Nilsvang, B. Ilshner, Acta. Metall. 37 (1989) 49-59.

57. B. J. Cane, Met. Sci. 13 (1979) 287-294.

58. C. Gupta, V. C. Elke, J. K. Chakravartty   Nucl Instrum Meth Res B 267 (2009) 3488-3490.

59. H. E. Evans   Mechanisms of Creep Fracture Elsevier Applied Science London (1984).

60. V. Sklenička, Kuchařová, M. Svoboda, L. Kloc, J. Buršík, A. Kroupa   Mater. Charact. 51 (2003) 35-48.

Table 1 The detailed chemical composition of the CB8 steel used for the investigation

Element	C	Si	Mn	S	P	Al	Cr
Amount (% wt)	0.17	0.27	0.2	0.006	0.009	0.026	10.86
Element	Mo	Co	Ni	V	Nb	N	B
Amount (% wt)	1.42	2.94	0.15	0.21	0.061	0.024	0.016
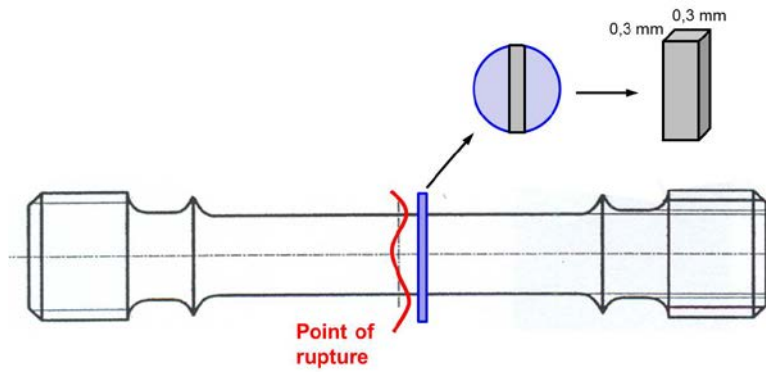
Figure 1.   A schematic of the creep test specimen showing the location of the sample extracted for carrying out SR-µCT.
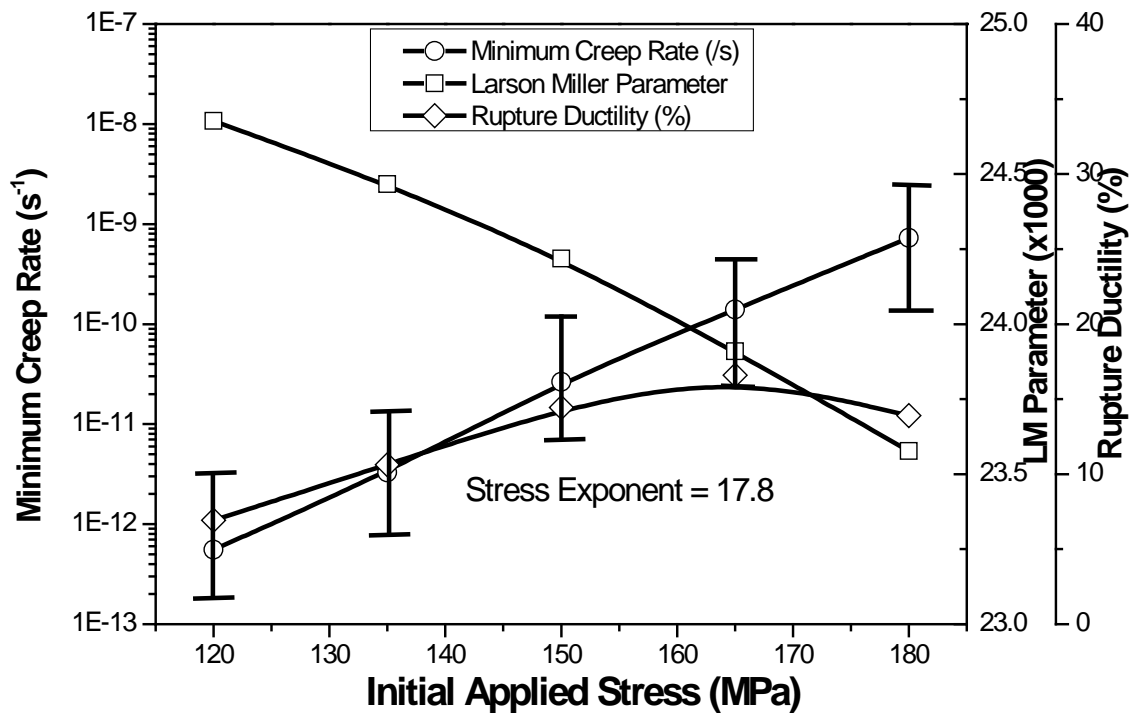
Figure 2 Plot showing the variation of minimum creep rate, Larson-Miller parameter, rupture ductility and diametral strain (reduction of area) with initial applied stress during the creep test.
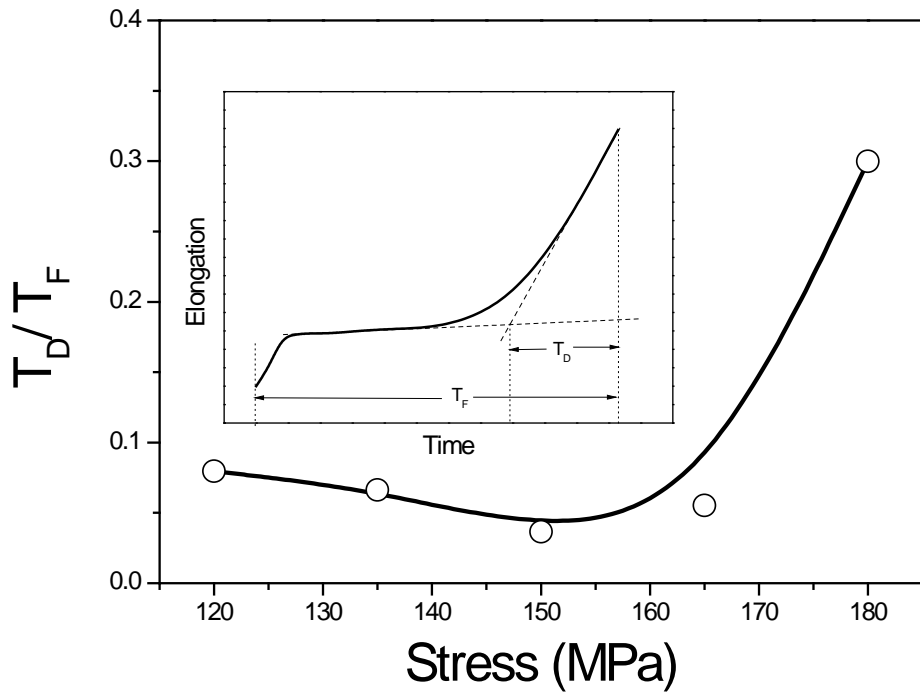
Figure 3. Plot showing the variation of fraction of creep life expended in the cavitation dominated region with initial applied stress during creep test. The inset shows the method of determining the ratio (T_D/T_F) from the elongation – time plot obtained from the creep test. T_D indicates the period of the creep life where cavitation dominated increase in creep rate occurs. T_F indicates the creep life obtained from the test.
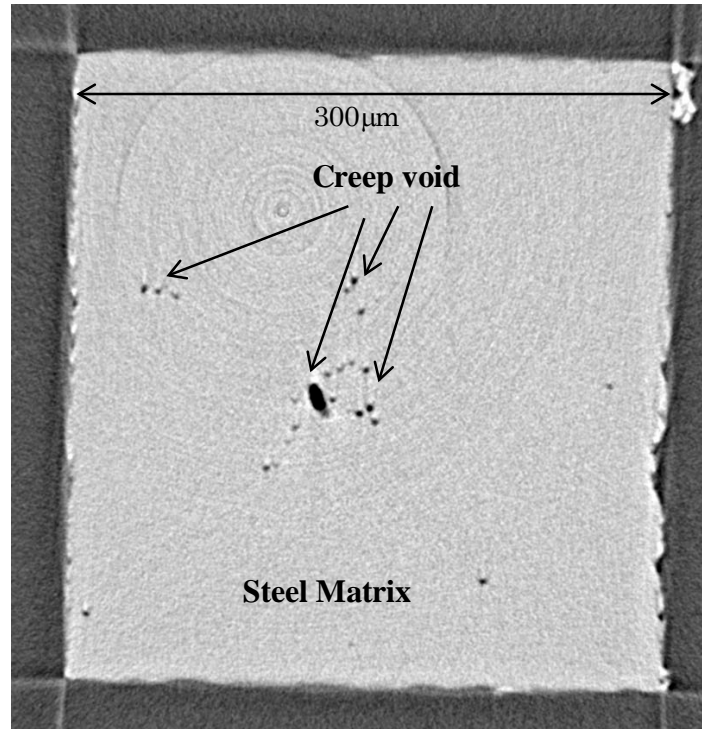
(a)
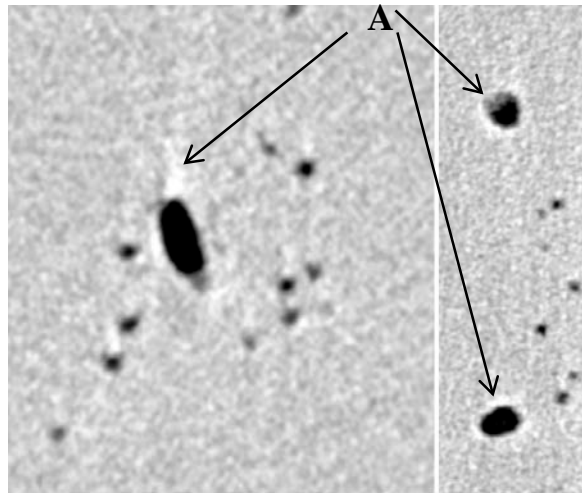
(b)

Figure 4   (a) A typical reconstructed slice obtained from SR-μCT scans on samples crept in the stress range 120 – 180 MPa containing creep voids. The crossesection of the steel matrix is 300 x 300 μm. (b) An enlarged view near the creep void regions showing the bright halo surrounding the matrix – void interface (indicated as arrows pointing towards A), which is a manifestation of the superimposition of the deflection contrast effects.
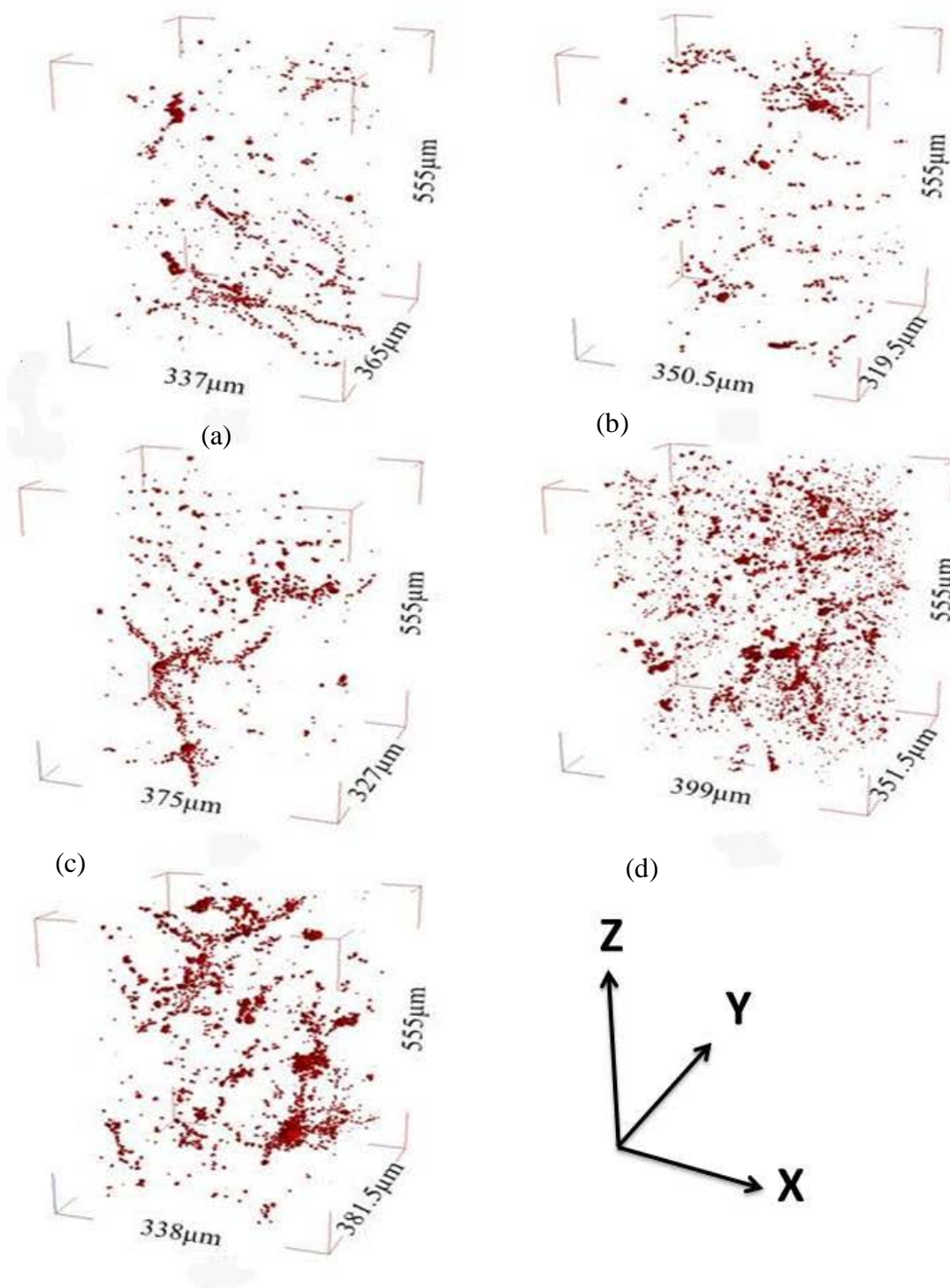
Figure 5. 3-D rendering of the region of interest subjected to tomography scan of samples extracted from creep specimens subjected to creep conditions of (a) 180 MPa/ 2825 hours (b) 165 MPa/ 6779 hours (c) 150 MPa/ 15316 hours (d) 135 MPa/ 29466 hours (e) 120 MPa/ 51406 hours
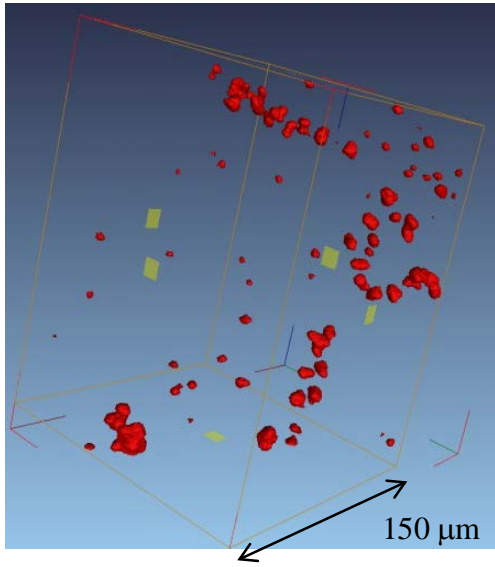
(a)
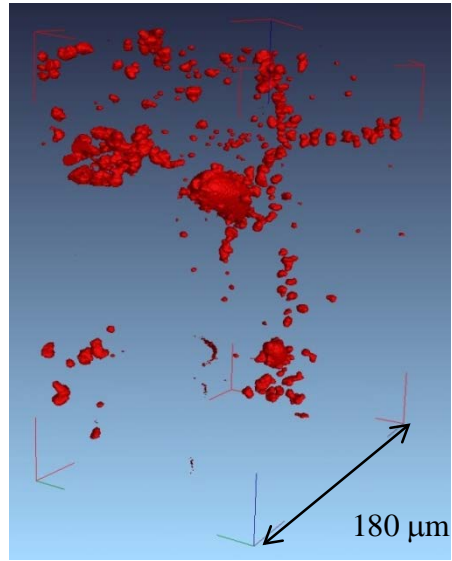
(b)
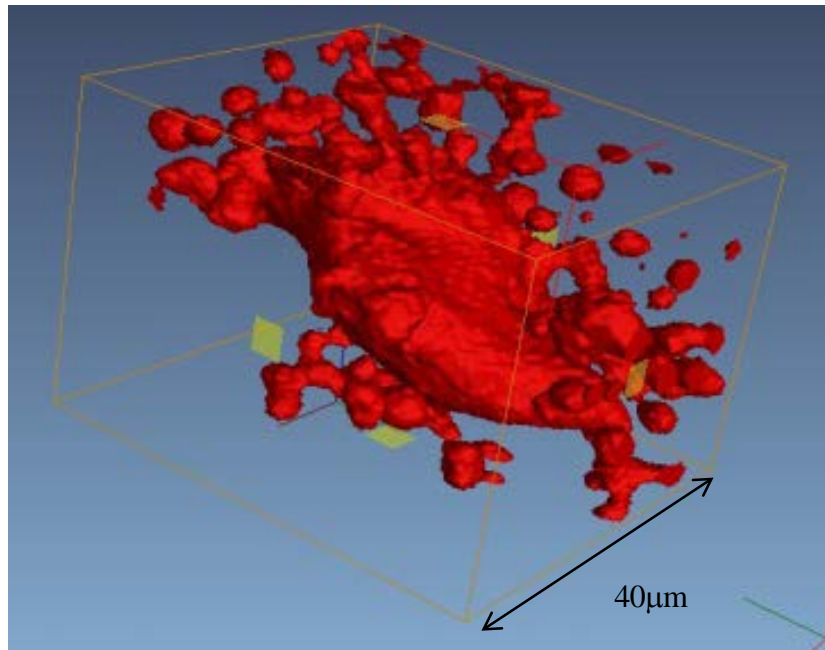
(c)

Figure 6. Types of shapes of creep voids obtained in the dataset obtained from sample crept at 120 MPa (a) sparsly distributed voids of multi lobed morphology (b) closely spaced chain of complex shaped voids arranged in a cluster near oblate shaped void (c) a large creep void of multi-lobed morphology.
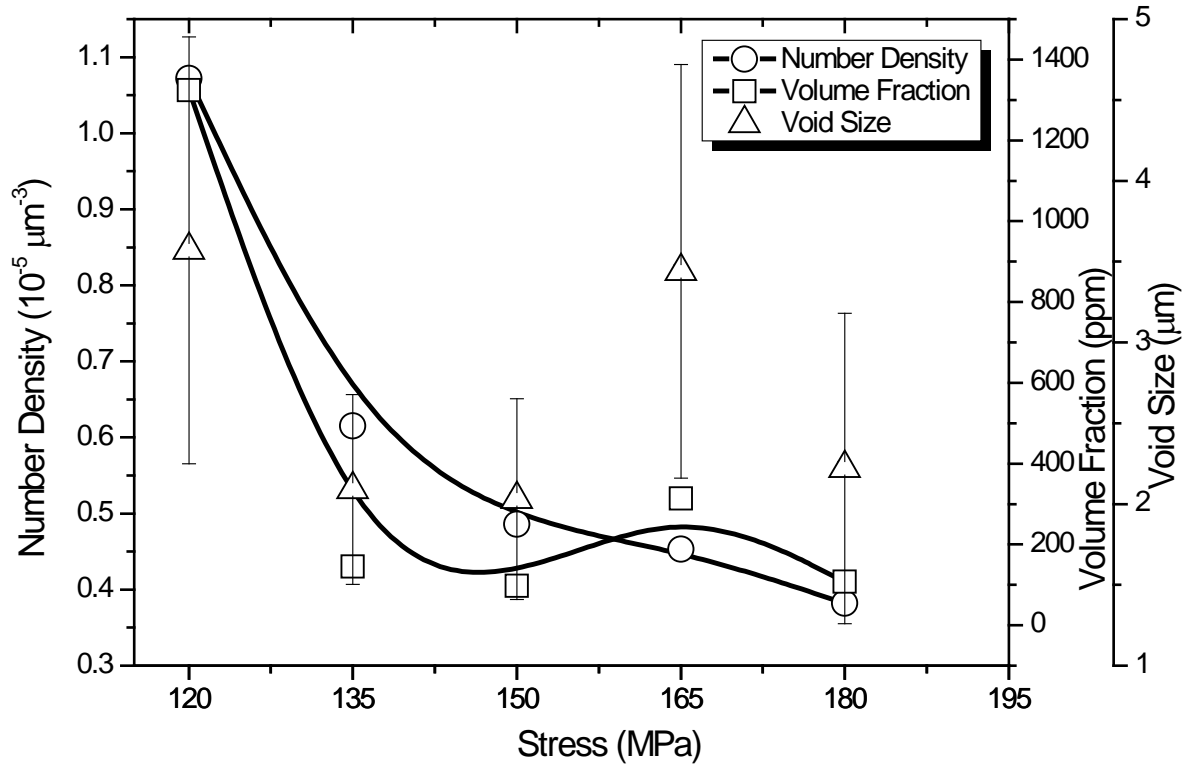
Figure 7   Plot showing the variation of number density, void volume fraction and void size with initial applied stress.
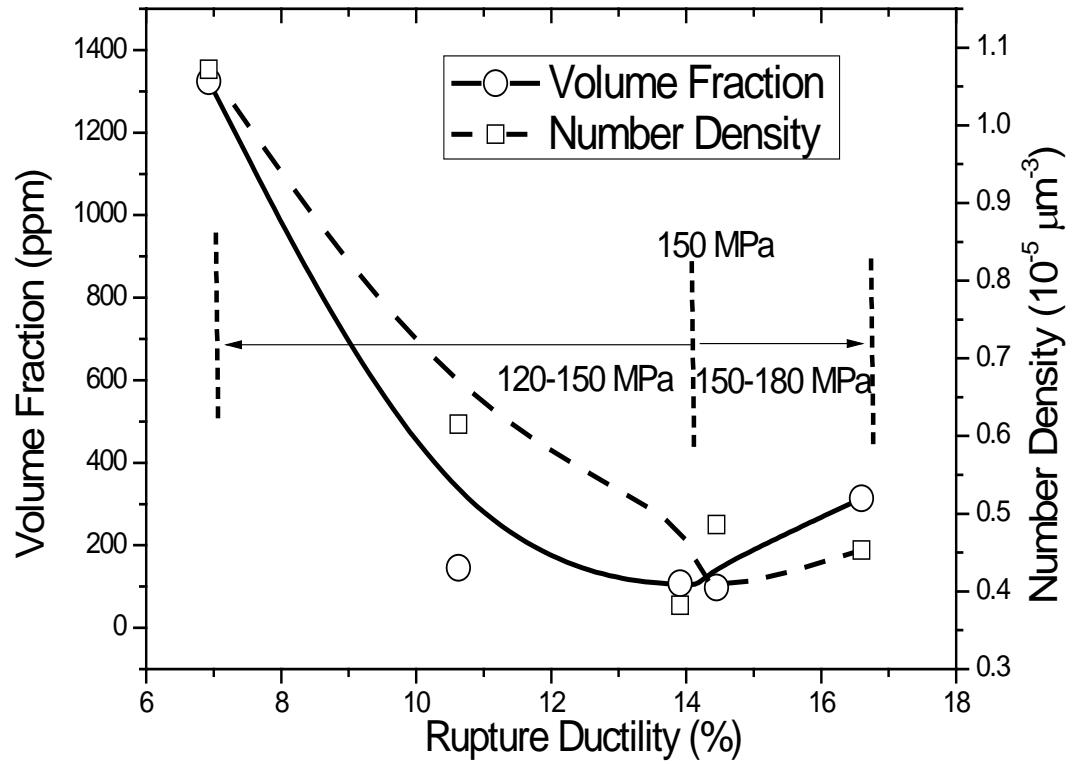
Figure 8 Plot showing the variation of cavitation characteristics – void volume fraction and number density with rupture ductility displayed by the CB8 steel over stress range 120 – 180 MPa.
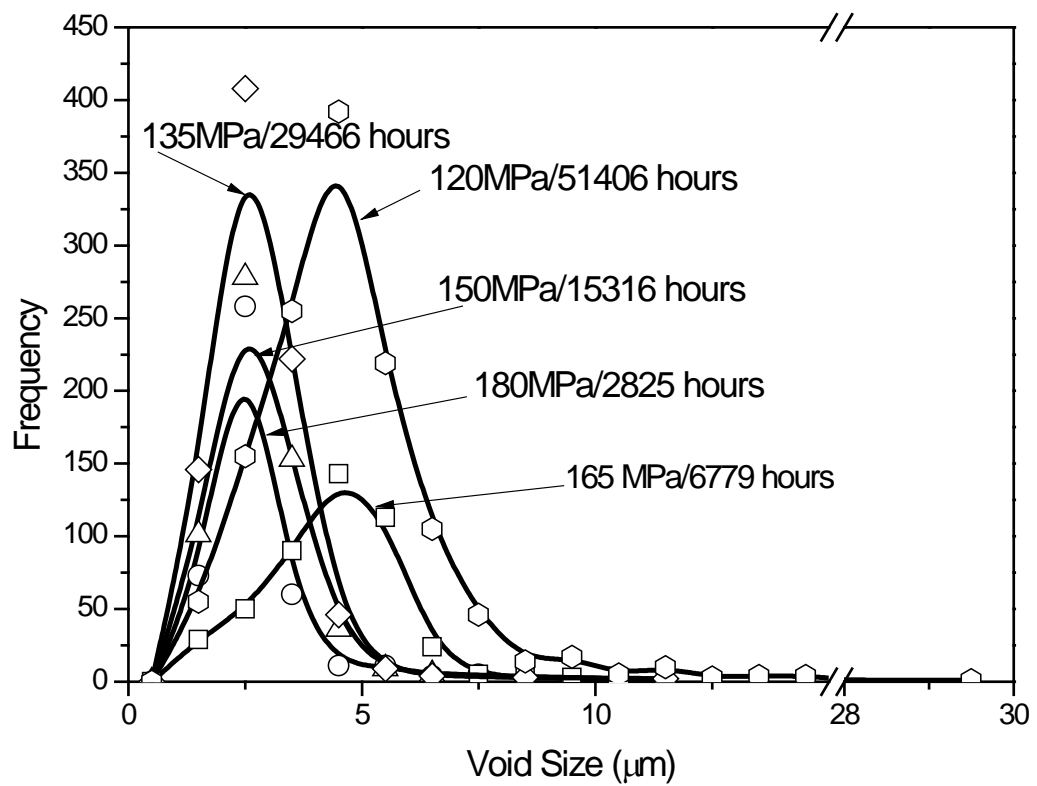
Figure 9 Plot showing the variation of void size distribution as a function of the creep conditions investigated in the study on CB8 steel.
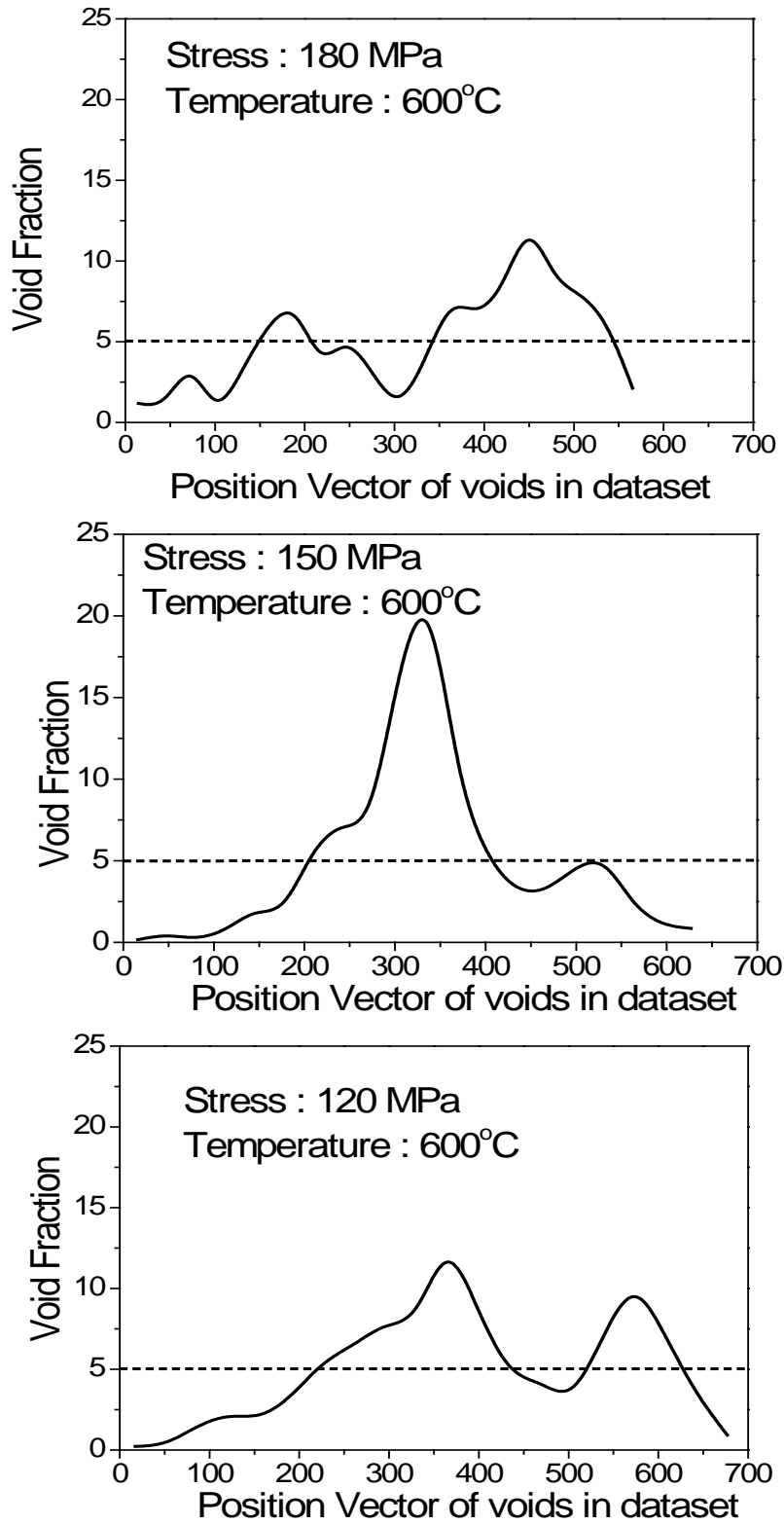
Figure 10 Plots showing the variation of local number fraction in 20 contiguous regions of the dataset corresponding to stresses (a) 180MPa (b) 150 MPa (c) 120 MPa
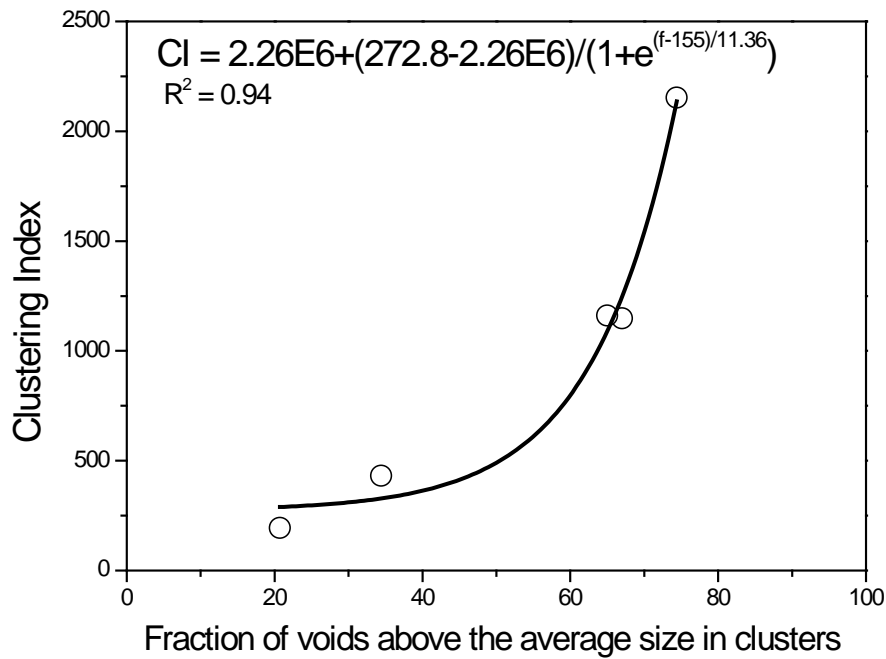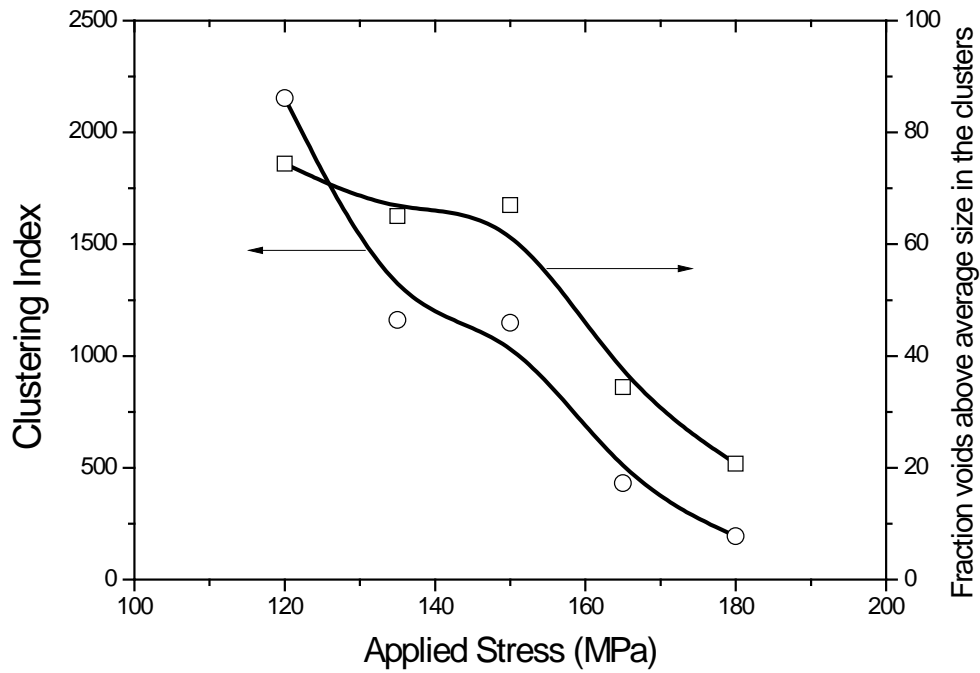
Figure 11 (a) Plot showing the variation of the clustering index and fraction of voids in the clusters above the dataset average, as a function of stress. (b) plot showing correlation and the fitting between clustering index and fraction of voids above the average size in clusters.
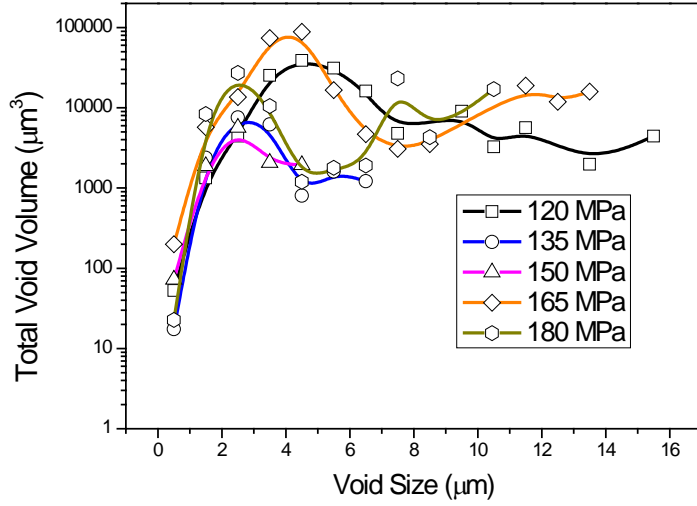
(a)
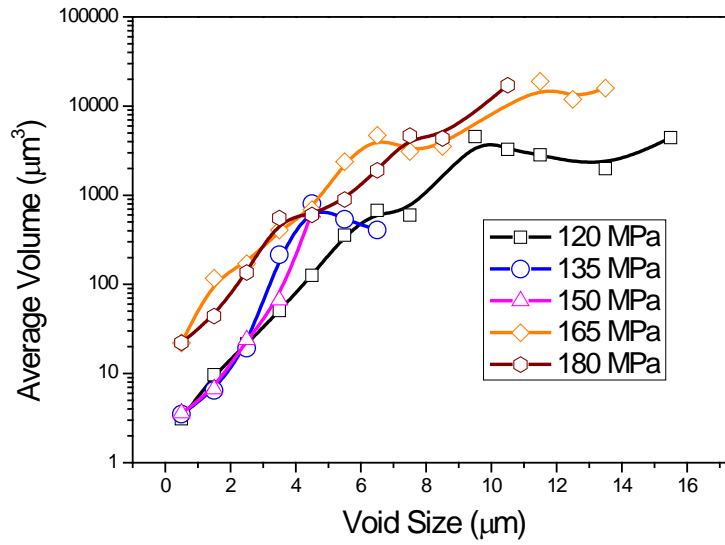
(b)

Figure 12 The plot showing the distribution of the (a) void volume fraction and (b) The plot showing the distribution of the average void volume over the void size for each of the datasets obtained from samples subjected to creep in the CB8 steel in the study.

.
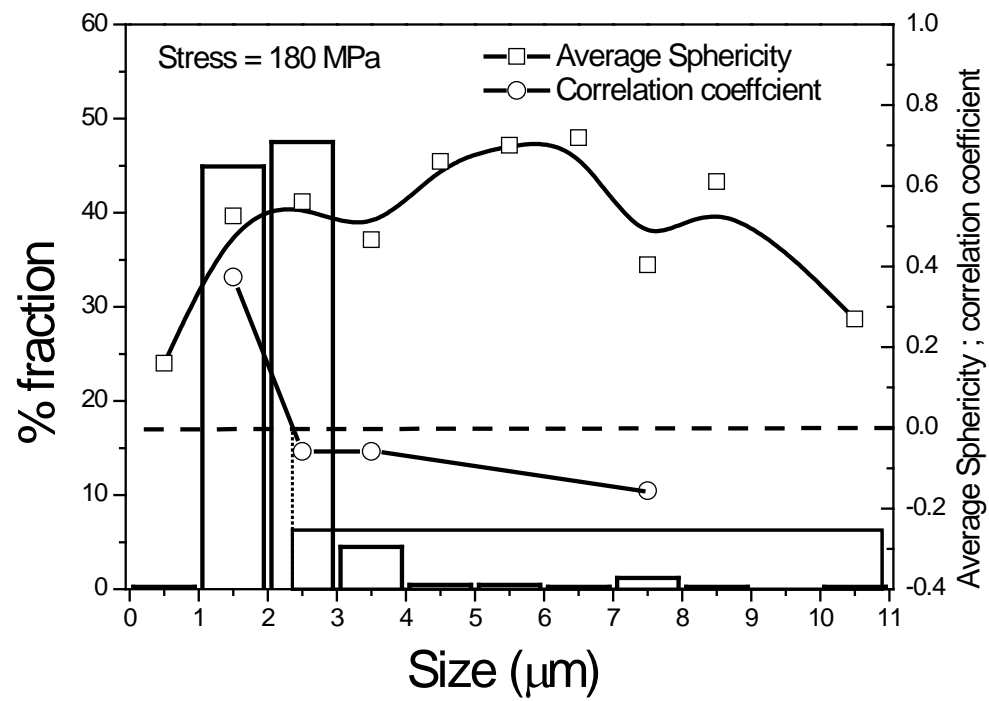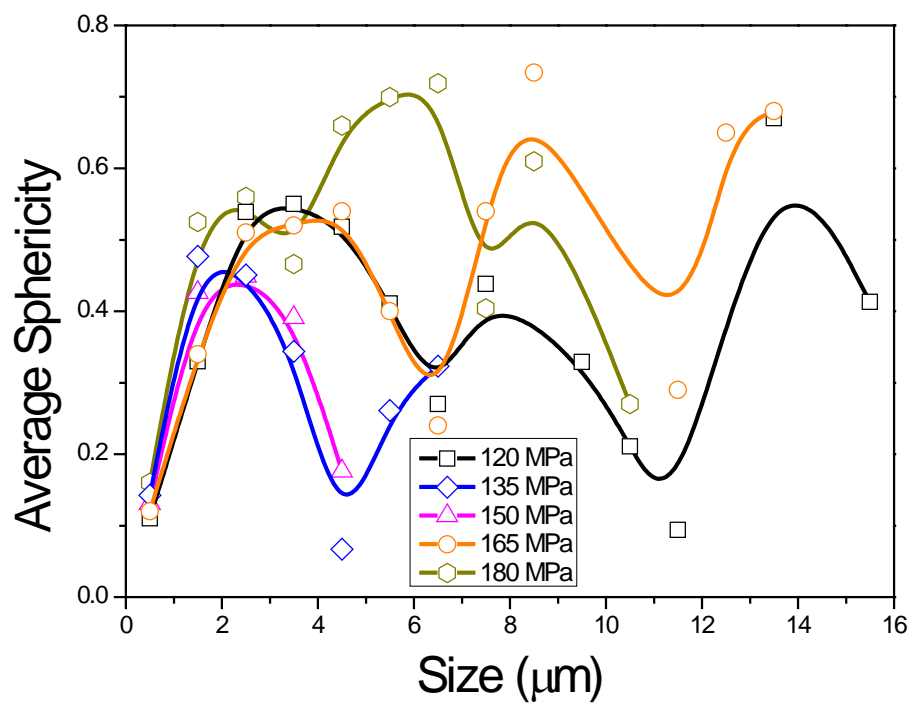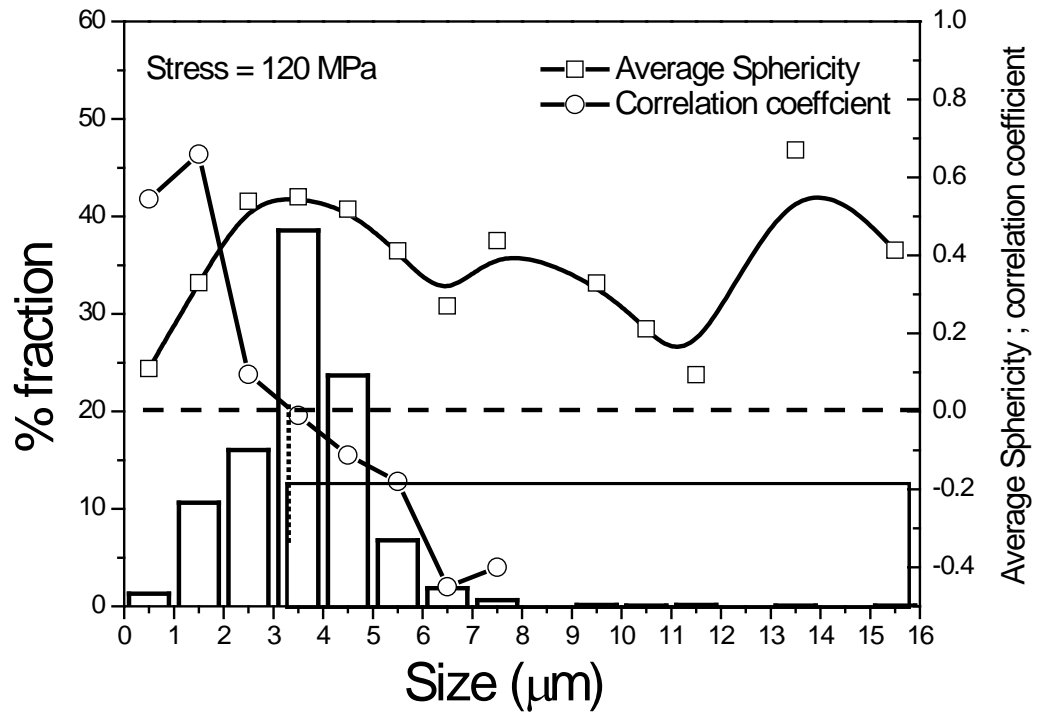
Figure 13 (a) average sphericity, over the void size for each of the datasets obtained from samples subjected to creep in the CB8 steel in the study (b) ; (c) The plot showing the distribution of the average sphericity over the void size for each of the datasets obtained from samples subjected to creep in the CB8 steel in the study. The shaded portion indicates the size range affected by coalescence.
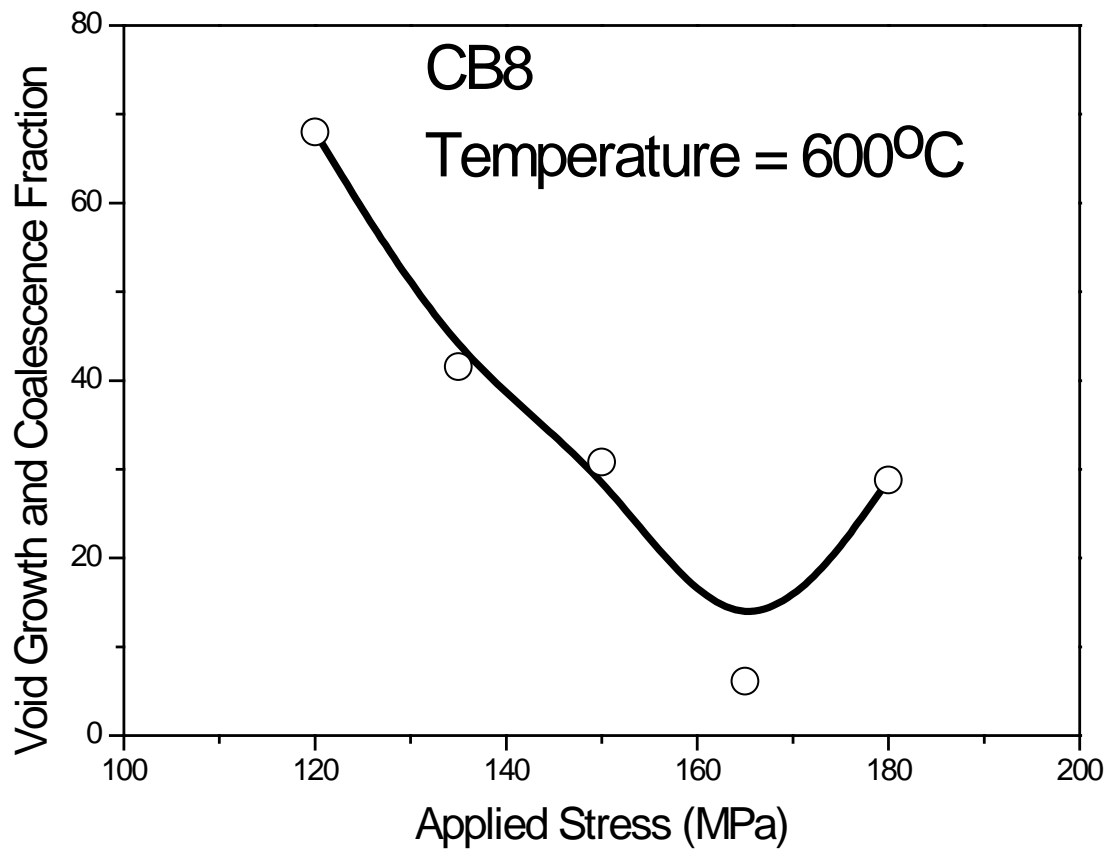
Figure 14. Plot showing the variation of the void growth and coalescence fraction in the datasets as a function of applied stress.
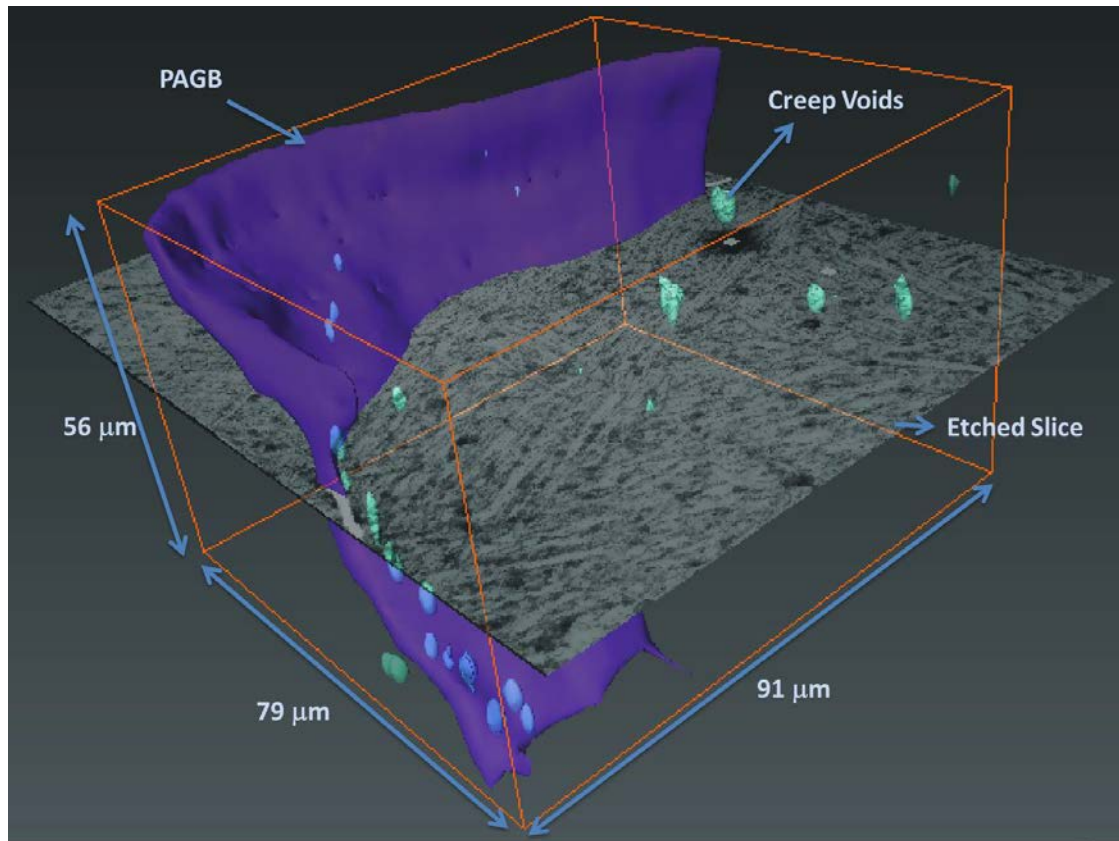
Figure 15 The composite 3D image obtained from serial sectioning carried out on the sample crept at 150 MPa, showing the reconstructed prior-austenite grain boundaries and creep voids.
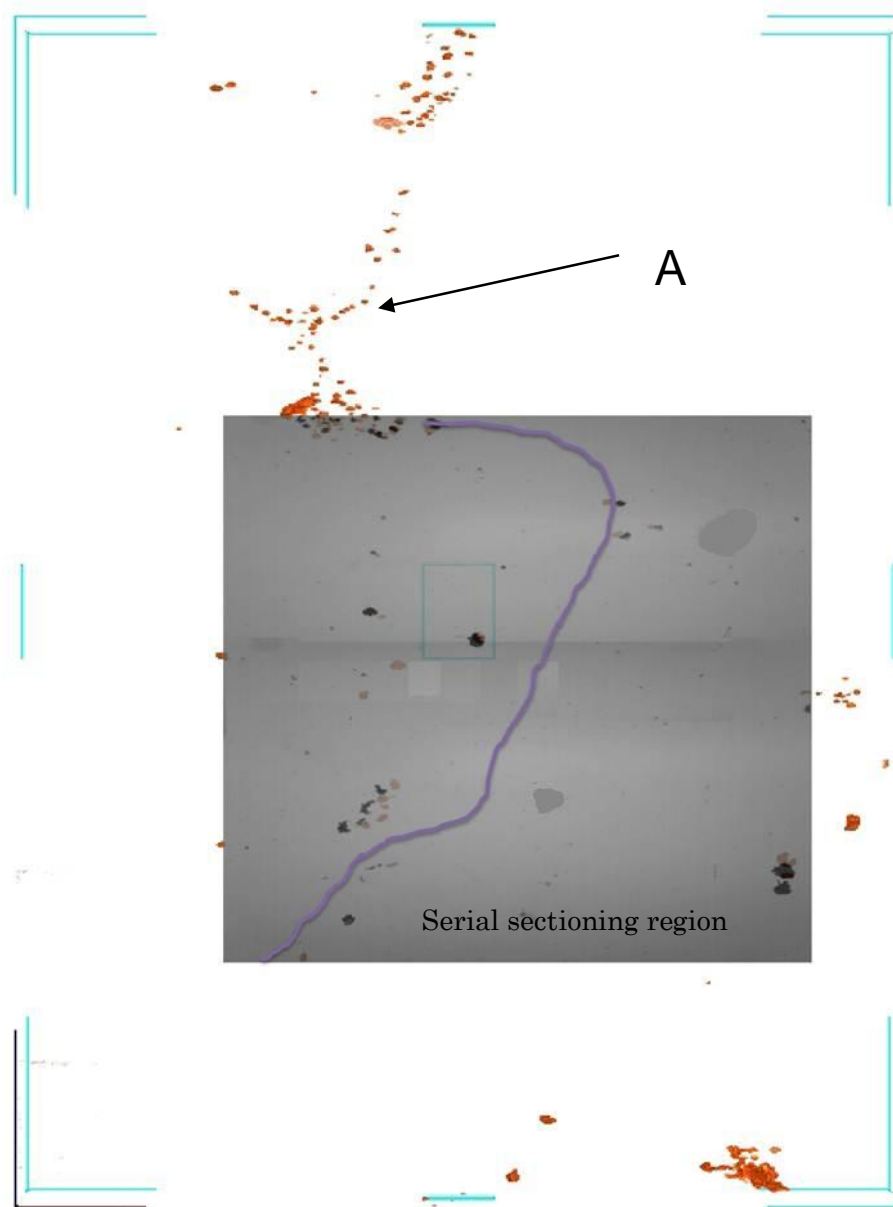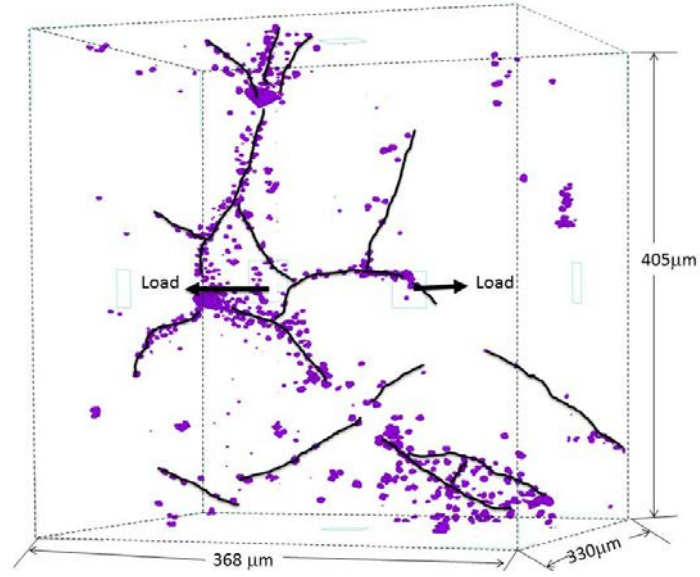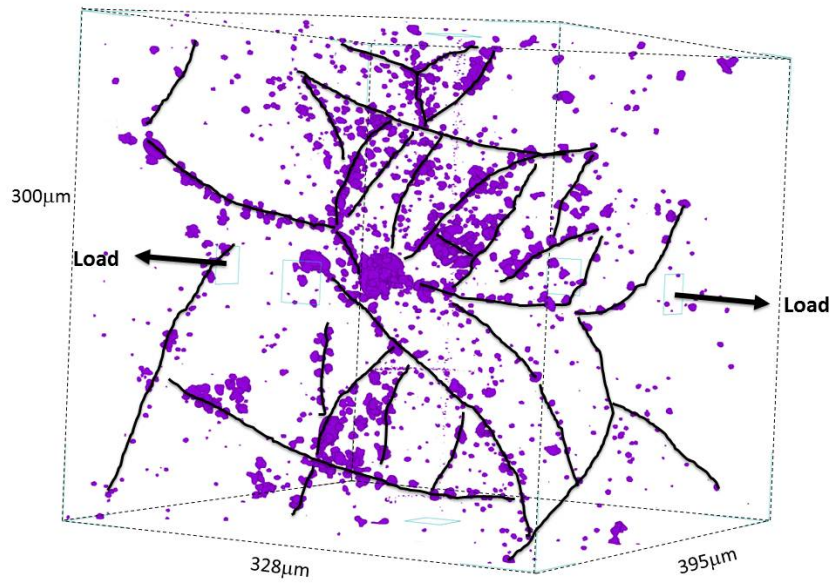
Figure 16 The composite image of the region characterized by serial sectioning located within the volume of sample characterized by micro-tomography scan. The dark line in the serial sectioning region corresponds to the location of the prior austenite boundary located 9 μm below the surface.

(a)

(b)

Figure 17 An expanded 3D rendering of the regions of higher number density of voids of the sample for the sample exposed to creep times of (a) 15316 hours (b) 51406 hours. The loci of the voids aligned within the reconstructed region of interest are shown by thin black lines.
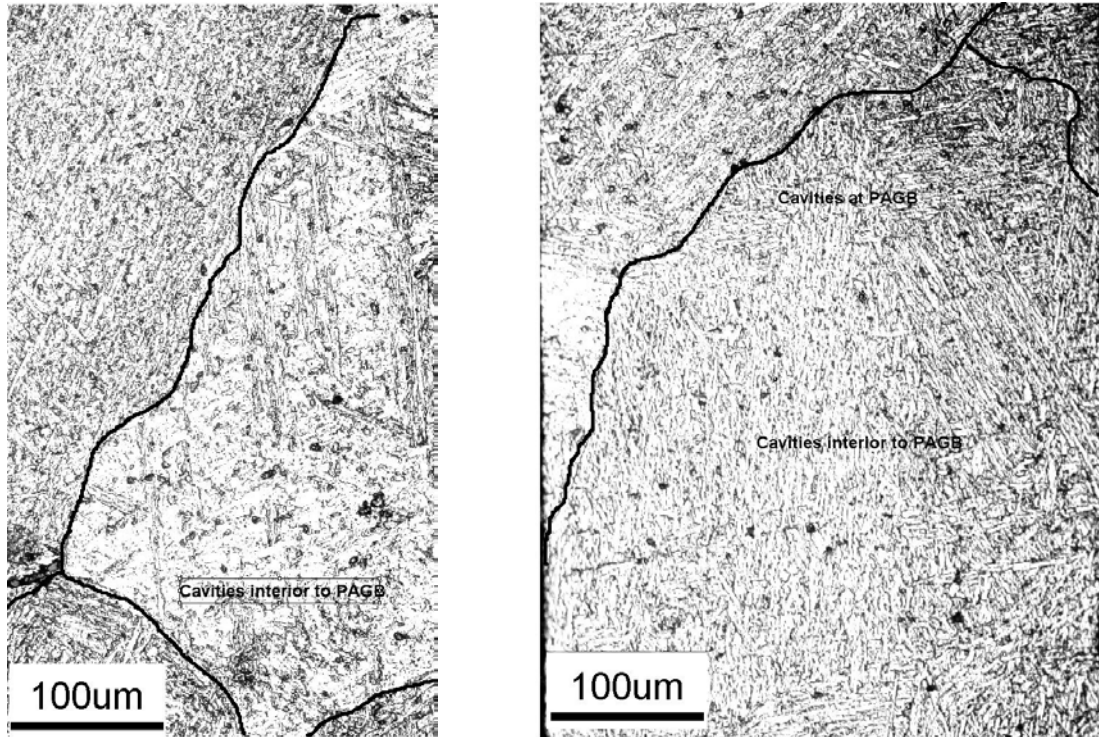
Figure 18.   Optical micrographs of two regions of the sample exposed to creep at 120 MPa showing the presence of grain interior cavitation. The prior austenite boundaries have been delineated by black lines.